Model~~l~~ling active layer thickness in permafrost rock walls ~~mountain permafrost~~based on an analytical solution of the heat transport equation, Kitzsteinhorn, Hohe Tauern Range, Austria.

Wolfgang Aumer[1,2], Ingo Hartmeyer[3], Carolyn-Monika Görres[1], Daniel Uteau[4], Maike Offer[5], Stephan Peth[~~5~~6]

[1]Geisenheim University, Department of Applied Ecology, Von-Lade-Straße 1, 65366 Geisenheim, Germany
[2]University of Kassel, Section of Ecological Plant Protection, Nordbahnhofstraße 1a, 37213 Witzenhausen, Germany
[3]GEORESEARCH Forschungsgesellschaft mbH, Wissenspark Salzburg-Urstein, Urstein Süd 13, 5412 Puch bei Hallein, Austria
[4]University of Kassel, Section of Soil Science, Nordbahnhofstraße 1a, 37213 Witzenhausen, Germany
[5]Technical University of Munich, Chair of Landslide Research, Arcisstr. 21, 80333 Munich, Germany
[~~5~~6]Leibniz University Hannover, Institute of Soil Science, Herrenhäuser Str. 2, 30419 Hannover, Germany

Correspondence to: Wolfgang Aumer (wolfgang.aumer@hs-gm.de)

Abstract. The active layer thickness (ALT) refers to the seasonal thaw depth of a permafrost body and in high alpine environments represents an essential parameter for natural hazard analysis. ~~is an essential parameter for natural hazard analysis, construction, land-use planning and the estimation of greenhouse gas emissions in periglacial regions.~~ The aim of this study is to model ~~the annual maximum thaw depth for determining~~ ALT based on bedrock temperature data measured in four shallow boreholes (SBs, 0.1 m deep) in the summit region of the Kitzsteinhorn (Hohe Tauern Range, Austria, Europe). We set up our heat flow model with temperature data (2016–~~-~~2021) from a 30 m deep borehole (DB) drilled into bedrock at the Kitzsteinhorn north-face. For modeling purposes, we assume 1D conductive heat flow and present an analytical solution of the heat transport equation through sinusoidal temperature waves resulting from seasonal temperature oscillations (damping depth method). The model approach is considered successful: In the validation period (2019–~~-~~2021), modeled and measured ALT differed by only 0.1±0.1 m, with a Root Mean Square Error (RMSE) of 0.13 m. We then applied the DB-calibrated model to four SBs and found that the modeled seasonal ALT maximum ranged between 2.5 m (SB 2) and 10.6 m (SB 1) in the observation period (2013–~~-~~2021). Due to small differences in altitude (~ 200 m) within the study area, slope aspect had the strongest impact on ALT. To project future ALT deepening due to global warming, we integrated IPCC climate scenarios SSP1-2.6 and SSP5-8.5 into our model. By mid-century (~ 2050), ALT is expected to increase by 48 % at SB 2 and by 62 % at DB under scenario SSP1-2.6 (56 % and 128 % under scenario SSP5-8.5), while permafrost will no longer be present at SB 1, SB 3 and SB 4. By the end of the century (~ 2100), permafrost will only remain under scenario SSP1-2.6 with an ALT increase of 51 % at SB 2 and of 69 % at DB.

1 Introduction

Permafrost is defined as ground (soil or rock and the water contained therein) that remains below zero degrees Celsius ~~frozen~~ for at least two consecutive years (Harris et al., 1988) and is warming on global scale (Biskaborn et al., 2019). In steep environments, such as the European Alps, warming-induced permafrost degradation is capable of destabilizing slopes and rock walls (Gruber et al., 2004; Gude and Barsch, 2005; Fischer et al., 2006; Gruber and Haeberli, 2007; Krautblatter et al., 2013). Consequently, permafrost degradation is considered as one of the main causes for natural hazards in high-alpine areas and is expected to play a significant role in triggering a wide spectrum of mass movements ranging from debris flows (Stoffel et al., 2014), to medium-scale rockfalls (Legay et al., 2021) to large-scale rock avalanches such as recently witnessed at the Piz Cengalo at the Swiss-Italian border (Walter et al., 2020) or in 2023 at the Fluchthorn (Austria). In general, European mountain permafrost is characterized by ground temperatures just slightly below the freezing point (warm permafrost), and as a result is highly climate-sensitive (Harris et al., 2009). Direct ground temperature measurements have shown, in some parts very fast, warming in the European Alps within the last decades (~~Harris, 2003;~~ Etzelmüller et al., 2020).

The active layer thickness (ALT) refers to the ground's thaw depth during the summer season. The seasonally thawed active layer is not permafrost by definition, but is a key parameter of permafrost bodies (Harris et al., 1988; Michaelides et al., 2019). In periglacial landscapes, geomorphological, ecological, hydrological and pedological processes take place almost exclusively within the active layer (Hinzman et al., 1991; Harris et al., 2009). ALT evolution over time thus represents a critical variable for hazard management and prevention, but also to accurately quantify greenhouse gas release from permafrost soils (Miner et al., 2022). Microbial activity and the decay of organic matter is restricted to the active layer. Consequently, ALT data provide required information to investigate carbon-climate feedbacks in earth system models (Mishra et al., 2017). They are also required for land-use planning and construction on permafrost to warrant foundation stability and to avoid infrastructure damage (Hjort et al., 2022). In high-mountain regions exceptional rockfall activity has been observed as a direct response to the thickening or new formation of the active layer during hot summers, which potentially exposes deep-seated failure planes to positive temperatures (e.g. Allen and Huggel, 2013; Ravanel et al., 2017). Due to its broad relevance across many disciplines, the Global Climate Observing System (GCOS, 2021) has recognized the ALT as an "Essential Climate Variable" (ECV), i.e., as a parameter that critically contributes to the characterization of Earth's climate (GCOS, 2021). ALT data are collected in a global database (GTN-P - Global Terrestrial Network for Permafrost) (Biskaborn et al., 2015), which reveals a worldwide trend towards ALT deepening (Biskaborn et al., 2019; Streletskiy et al., 2020; Kaverin et al., 2021).

Complex mountain topography (altitude, slope aspect, inclination) significantly modifies the amount of incoming solar radiation received by the ground surface. It thus has a pronounced effect on surface net energy input and leads to a high spatial variability of subsurface temperatures (Haeberli et al., 2010; Gubler et al., 2011). As a result, ALT varies strongly at the same elevation, ranging from a few meters to more than ten meters (PERMOS, 2023). ALT can be precisely recorded through temperature measurements in deep boreholes. High-alpine drilling works are, however, technically challenging, expensive and time-consuming, and only provide point recordings with limited spatial representation. The implementation of shallow boreholes (SBs) to record near-surface temperature (e.g. at 0.1 m depth), however, is simpler and allows significantly more measurement points (Hartmeyer et al., 2012), yet provides no direct ALT recordings due to an insufficient penetration depth. In this study, we used near-surface temperature data (0.1 m depth), which is widely available in permafrost regions, to simulate ALT based on the heat transport equation.

A comprehensive overview of various permafrost heat flow modeling approaches is provided in the review paper by Riseborough et al. (2008). So far numerous studies of lowland (e.g. Burn and Zhang, 2009; Etzelmüller et al., 2011) and mountain permafrost (e.g. Engelhardt et al., 2010; Hipp et al., 2012) have simulated heat flow and ALT using 1D numerical models, which are well-suited to handle heterogenous material properties. For the first time, here we present~~ed~~ an analytical solution to the heat transport equation for 1D ALT modeling in permafrost-affected rock walls ~~to model ALT in mountain permafrost at the~~ (borehole scale). Analytical solutions provide a direct mathematical description of the relationship between variables and therefore offer a concise, process-based understanding how (modified) input parameters impact the studied system. This is of particular relevance in global-warming-related sensitivity analyses to estimate to which extent changes in input parameters (e.g. rising temperatures) impact the result of a model without the need for extensive simulations. Following De Vries (1963), we analytically solved the heat transport equation through sinusoidal thermal waves which propagate into the subsurface. A six-year dataset from a 30 m deep borehole (DB) at the Kitzsteinhorn (Austria) served as data base for model calibration and validation. The model was then used to simulate present-day ALT at four SBs (0.1 m deep) located in the same study area, assuming identical thermal properties due to highly similar bedrock properties. In addition, we integrated IPCC (Intergovernmental Panel on Climate Change) climate projections (IPCC, 2023) into our model to simulate the ALT for mid and end of the century. The new approach was applied to a single mountain (Kitzsteinhorn summit pyramid), but is well-suited for modeling~~to model~~ ALT at~~on~~ larger scales in ~~complex high-mountain topography~~ steep bedrock environments.~~ as well as in less complex (sub)polar lowland topography.~~

2 Study Area

The Kitzsteinhorn is part of the Hohe Tauern mountain range in the Central Eastern Alps (Austria). The highest point is at 3,~~ ~~203 m a.s.l. (47°11'17"N, 12°41'15"E). Because of the relative singularity of the mountain massif and a pyramidal summit structure, the study area is well suited to investigate the influence of slope aspect and elevation on ground temperature~~s~~. The climate at the Kitzsteinhorn, which is located just north of the main alpine ridge, is characterized by humid, high-alpine weather conditions (Otto et al., 2012). In the vicinity of the study area (< 2 km), three weather stations are located at different altitudes. The stations at Glacier Plateau (GP) and Kammerscharte (KS) are closest to the boreholes investigated in this study, and annual air temperature of these two stations are highly~~very~~ similar (Table 1). Minimum temperatures occur in January and February, maximum temperatures in July and August.~~ Table 1 summarizes the key information from the weather stations.~~

In the study area, permafrost distribution was simulated using the empirical-statistical model "PERMAKART 3.0", which estimates permafrost probability using a topo-climatic key for the Hohe Tauern mountain range (Schrott et al., 2012). Based on this simulation, permafrost can be expected with a ~~very~~ high probability (> 75 %) ~~in~~ for north-facing rockwall sections in ~~an area of ~ 1.2 km² around~~ the summit region. ~~Permafrost predominantly occurs on the northwest flank and, to a slightly lesser extent, on the northeast flank.~~ In contrast, no significant ~~occurrences of~~ permafrost occurrence is ~~are to be~~ expected on the south-facing~~exposed~~ mountain slopes~~flanks~~ (Fig. 1).

Most of the bedrock in the study area is made up of gray-blue (freshly fractured) and yellow-brown (with incipient weathering) calcareous mica schist (Krainer, 2005). Tectonic stress in combination with intense physical weathering has led to the formation of joints with large apertures (Hartmeyer et al., 2012). Optical borehole imaging carried out at the deep borehole (DB) immediately after drilling showed joint sizes apertures of a few mm up to several cm (usually < 5 cm) in the first couple of meters of the borehole. With increasing depth, the calcareous mica schist becomes more compact. Due to the schistosity, dipping steeply (~ 45°) towards north, the rock has an anisotropy for water and heat transport. To quantify bedrock pore volume, seven core samples from the study area (Fig. C1) were weighed after six weeks of water saturation and after drying at 105 °C over 24 hours to achieve a constant weight. The resulting effective porosity (ϕ_{eff}), which includes only the hydraulically connected pores (Sass, 2005) ranged from 0.3–0.4 % (Table C1). Furthermore, the sum of connected and unconnected pores was quantified by determining the samples' matrix volume (V_m) with a helium pycnometer (AccuPyc II, Micromeritics Instrument Corp., USA). The derived (total) porosity (ϕ) ranged from 0.4–1.0 %.

The study area hosts a long-term geoscientific monitoring project ("Open-Air-Lab Kitzsteinhorn") which was initiated in 2010 and investigates the impact of global warming on permafrost thaw and rock stability based on a combination of subsurface, surface and atmospheric measurements (Hartmeyer et al., 2012; Hartmeyer et al., 2020a; Hartmeyer et al., 2020b). The present study is based on the existing research infrastructure and uses bedrock temperature data from a 30 m deep borehole (DB) and four shallow boreholes (SBs, 0.1 m deep)~~, three of which are located in the immediate vicinity of the Kitzsteinhorn summit~~ (Table 2, Fig. 1).

DB is situated approximately 50 m below the local cable car top station in a thermally undisturbed, north-facing rock slope section with a 45° average gradient. The SBs were selected based on slope aspect, altitude, accessibility and data availability (numerous DB sites in the area could not be used for the present study due to significant data gaps related to lightning strike damage). SB 2 (NW), SB 3 (ENE) and SB 4 (SE) are located in the immediate vicinity of the Kitzsteinhorn summit. Due to their almost identical altitude (~ 3,200 m a.s.l.) this SB trio is well-suited to specifically study the impact of slope aspect on ALT. SB 1 (similar slope aspect as SB 2) and DB are situated around ~ 200 vertical meters below SB 2–4 and represent an interesting contrast to investigate altitudinal effects.

Table 1. Weather data from ~~the~~ three nearby (< 2 km) ~~different~~ weather stations Alpincenter (AC), Gletscherplateau (GP) and Kammerscharte (KS) ~~in the vicinity of the study area (< 2 km)~~, MAAT: mean annual air temperature (period 2011–2021).

Station	Altitude a.s.l (m)	MAAT (°C)	Slope of temperature over 10 a (°C)	Max. snow depth (m)	Mean global radiation (W m^{-2})
AC	2,446	1.3	0.7	4.8	NA
GP	2,920	(-2.3)	NA	(5.8)	NA~~(158)~~
KS	2,561	-2.3	0.7	3.7	158~~NA~~

~~Data are daily mean values in the observation period from 01.01.2011 to 31.12.2021; data at the weather station GP for the years 2018, 2019 and 2020 are missing due to measurement failures (values in brackets)~~Values for GP are given in brackets due to gaps in the period 2018–2020; NA: not available.

Table 2. Borehole locations and temperature logging depths ~~in the study area~~.

Name	Altitude a.s.l (m)	Temperature sensor depths (m)	Slope aspect (°)	Inclination angle (°)
DB	2,990	0.1, 1, 2, 3, 5, 7, 10, 15, 20, 25, 30	0 (N)	45
SB 1	2,981	0.1	285 (WNW)	60
SB 2	3,192	0.1	315 (NW)	40
SB 3	3,196	0.1	65 (~~O~~ENE~~O~~)	80
SB 4	3,198	0.1	160 (SE~~O~~)	45

Altitude a.s.l. refers to the ~~entrance or the highest point of the boreholes~~borehole mouth. The boreholes were drilled perpendicular to the local inclination angle (DB: Deep borehole, SB: Shallow borehole).

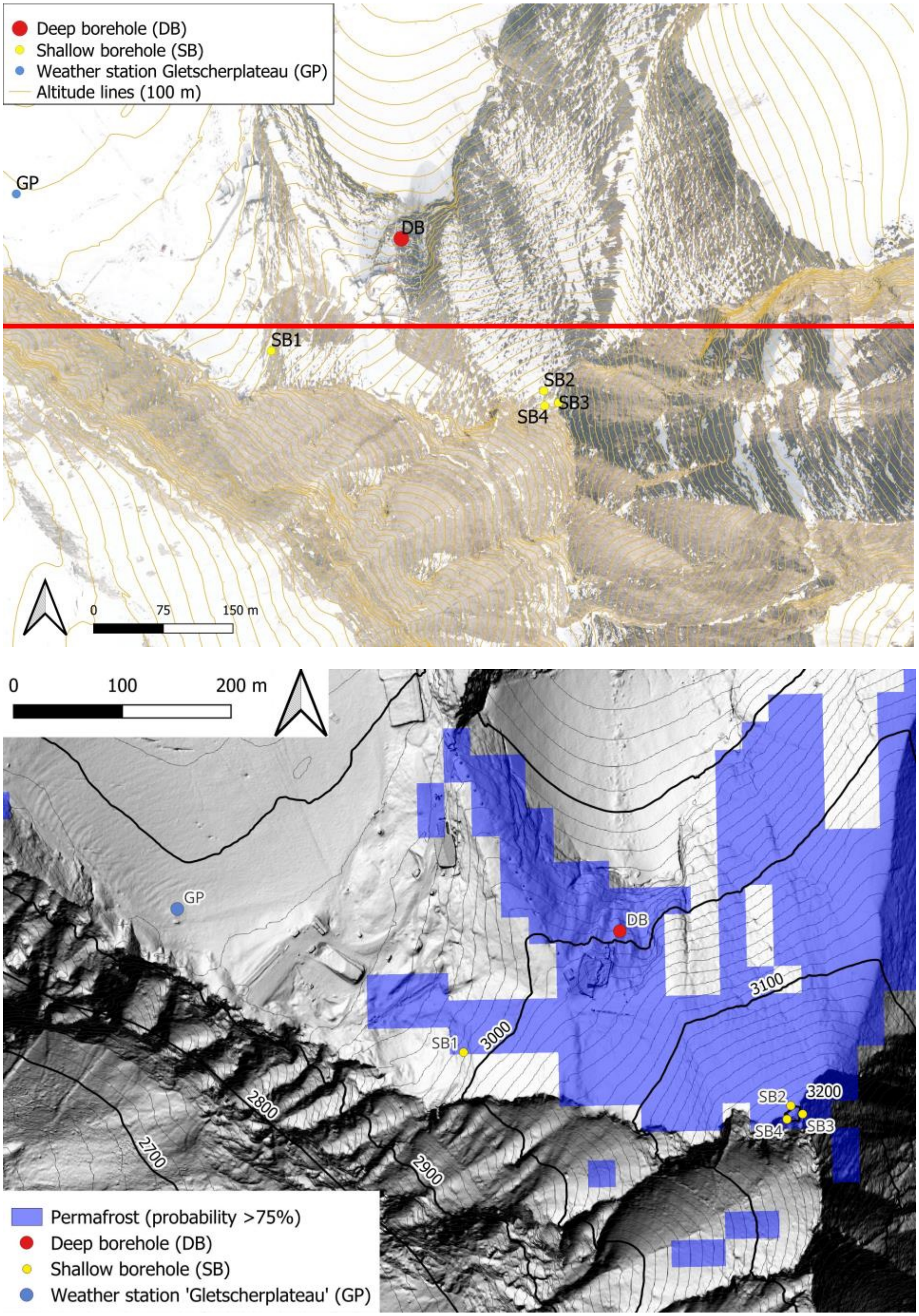

Figure 1: Borehole locations for temperature logging in the Kitzsteinhorn study area. The thermal model used to estimate active layer thickness (ALT) was calibrated and validated on the deep borehole (DB).~~ Orthophoto and altitude lines: www.basemap.at.~~ Permafrost probability, derived from the empirical-statistical model 'Permakart 3.0' (Schrott et al. 2012), is high for north-facing rock slope sections in the summit region.

3 Material and Methods

3.1 Temperature logging and data processing

The deep borehole (DB) was drilled with an air rotary drilling equipment (diameter 90 mm) to a depth of 30 m (Fig. 2a and 2b). The borehole was then instrumented with an innovative temperature measurement system consisting of a PVC-casing with brass segments at the designated sensor depths (Hartmeyer et al., 2012). Upon insertion of the thermistor chain, all temperature sensors establish direct contact with the casing's brass segments. Due to the high thermal conductivity of the brass segments (~ 110 W m^{-1} K^{-1}) this setup enables excellent thermal coupling between the temperature sensors and the surrounding bedrock~~ (annulus was filled up with concrete)~~. The annulus was filled up with concrete to avoid water entry and potential ice formation. This most likely has a negligible effect on heat conduction between temperature sensors and ambient rock for the following reasons: (i) due to the 45° drilling angle the entire casing rests on the borehole 'floor', the bottom side of the casing is therefore in permanent physical contact with the surrounding bedrock; (ii) thermal conductivity differs only slightly between concrete (~ 2 W m^{-1} K^{-1}) and schists (~ 3 W m^{-1} K^{-1}) (Talebi et al., 2020; Balkan et al., 2017). Temperature inside the DB is measured with high-precision Pt100 thermistors with an accuracy of ±0.03°C between -50 °C and 400 °C (Platinum Resistance Temperature Detector L220, 1/10 B, Heraeus Sensor Technology®, DE).

In addition to the DB, we used ground temperature data measured in four shallow bedrock boreholes (SBs) ~~, diameter 18 mm).~~ which were drilled to a depth of 0.1 m (diameter 18 mm). All SB locations are characterized by (i) a compact rock mass without significant joints, (ii) a uniform microtopography ('clean' slope aspect), and (iii) the absence of an unconsolidated sediment cover (Fig. 2). ~~The SBs were drilled to a depth of 0.1 m (Fig. 2b) and equipped with miniature temperature sensors. Prior to the installation, t~~The used temperature sensors (IButton®, DS1922L, Maxim Integrated Products®, USA) were glued to PVC rods (17 mm diameter) and ~~then~~ inserted into the SBs. After insertion, the borehole entrance was sealed watertight with silicone. The ~~used~~ sensors ~~(Ibutton®, DS1922L, Maxim Integrated Products®, USA)~~ consists of a button cell (steel housing) with an integrated computer chip, real-time clock and temperature sensor with an accuracy of ±0.5 °C within the temperature range -10 to 65 °C. Extensive empirical testing with iButtons®, however, yielded an absolute sensor accuracy of ±0.21 °C, underlining their suitability for high-quality thermal monitoring (Hubbart et al., 2005).

For model development (calibration and validation), DB daily mean temperature was used for the period 01 January 2016 to 31 December 2021. Daily mean values were determined based on twelve measurement points per day. Temperature data were spline-interpolated (Δz = 10 cm) for better depth resolution between measurements. Due to polynomial adjustments of the spline interpolation, positive interpolation values (< 0.1 °C) between two negative measurement values occurred in 39 cases. Since these interpolation values were not realistic, they were set to 0 °C. The depth z (m) and time t (day) of the year where temperature T(z,t) was above 0 °C were estimated from the measured and interpolated depth- and time-dependent temperature data; daily thaw depths were derived subsequently. Model applications at the SBs were based on temperature records in the period 01 January 2012 to 31 December 2021, however, large data gaps existed in some cases. Temperature in the SBs was recorded every three hours (hourly measurements could not be implemented due to limited memory space on the iButton®) and resulted in eight measurement points per day for daily mean temperature calculations. (Note that in the whole study the mathematical sign plus minus (±) between two values stands for standard deviation.)

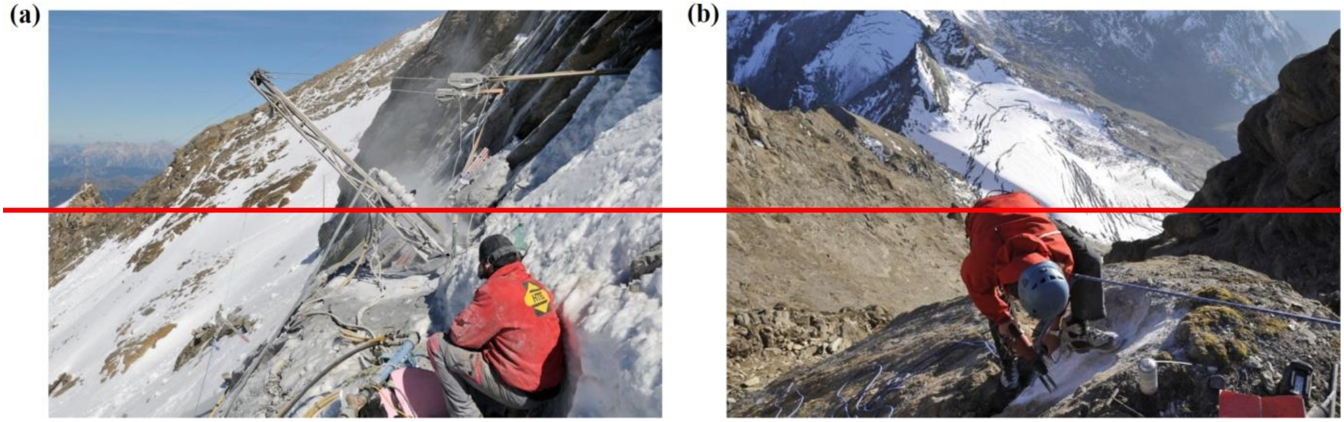

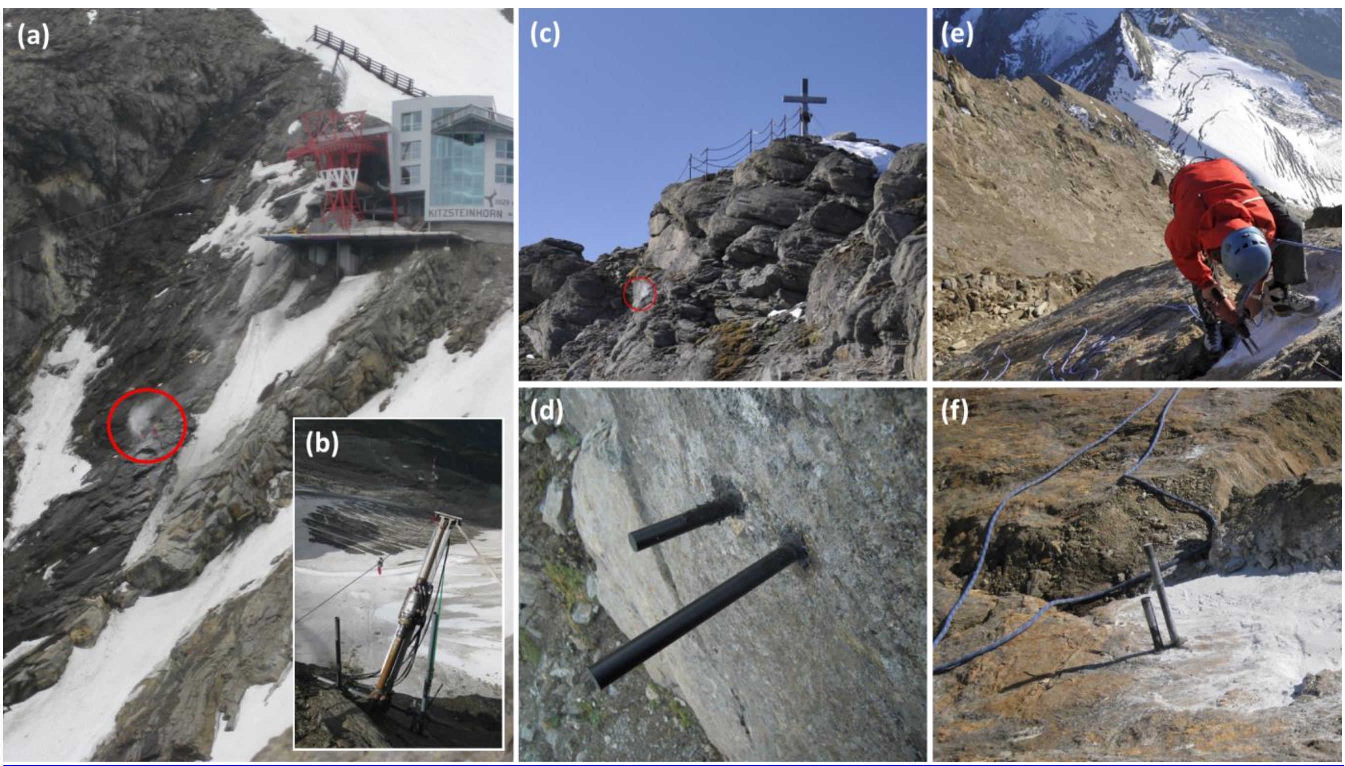

Figure 2: (a) Drilling works at DB in the Kitzsteinhorn north-face (07.07.2011); (b) Drilling equipment at DB (17.08.2011); (c) Location of SB 3 below the Kitzsteinhorn summit (06.10.2011); (d) Close-up of SB 3 (31.07.2013); (e) Drilling works at SB 4 (05.10.2011); (f) Close-up of SB 4 (05.10.2011) (all photos taken by I. Hartmeyer).~~(a) Drilling procedure (air-flushed rotary drilling) for a 30 m deep borehole (DB) on the western flank of the Kitzsteinhorn (Austria) (identical procedure to the DB used in this study). (b) Drilling of a shallow borehole (SB) for the installation of Ibuttons® for temperature logging at a depth of 0.1 m on the southern flank of the Kitzsteinhorn (2011). Due to the lower effort, more measuring points could be realized to address spatial variability. Photos by Ingo Hartmeyer.~~

3.2 Thermal modelling

Conduction was assumed to be the only transport mechanism of heat flow, thus neglecting convection and latent heat release. Conductive heat transport can be described by the heat transport equation, which describes temperature change as a function of space and time (Williams and Smith, 1993):

$$\frac{\partial T}{\partial t} = \alpha \frac{\partial^2 T}{\partial z^2} \quad (1)$$

with ∂T/∂t being the first derivative with respect to time (Δt (s)), α is the thermal diffusivity ($m^2\,s^{-1}$) and $\partial^2 T/\partial z^2$ is the second derivative in respect to position ~~(Δz (m))~~ in terms of depth (Δz (m)) ~~(z)~~. The thermal diffusivity α ($m^2\,s^{-1}$) is defined as the quotient of the thermal conductivity λ ($J\,s^{-1}\,m^{-1}\,{}^{\circ}C^{-1}$) and the specific volumetric heat capacity C_V ($J\,m^{-3}\,{}^{\circ}C^{-1}$):

$$\alpha = \lambda / C_v \quad (2)$$

In our study, the heat transport equation was solved following an analytical approach: Under the assumption of a homogeneous ground, a harmonic sinusoidal temperature oscillation, and a mean ground temperature (T_m) that is constant with depth (z), the heat transport equation (Eq. 1) could be solved in one-dimension (z). The periodic temperature profile on the surface (z = 0) can be described as a function of time with the following sine function (DeVries 1963):

$$T_s = T_m + A_s \sin\left[\left(\frac{2\pi}{P}\right)(t - t_m)\right] \quad (3)$$

where T_s is the time dependent temperature at the surface (°C), T_m is the mean temperature at the surface in an annual or daily cycle, A_s is the temperature amplitude on the ground surface (°C), P is the period length (s), t is the time in the annual or daily cycle (s), and t_m (s) is the time in the period when $T_s = T_m$ (during the rise in temperature within a period). Given the set constraint of a constant mean ground temperature at each depth, a time-dependent temperature function for arbitrary depths could be established by using the sinusoidal function from Eq. 3:

$$T_{(t,z)} = T_m + A_s \exp^{\left(\frac{-z}{d}\right)} \sin\left[\left(\frac{2\pi}{P}\right)(t - t_m) - \frac{z}{d}\right] \quad (4)$$

Where $T_{(t,z)}$ is the temperature (°C) that depends on time ~~(~~t~~, in~~ (s)~~econds)~~ and depth ~~(~~z~~, in~~ (m)~~eters)~~, d stands for the damping depth (m) and denotes the depth at which A_s has been damped to 37% while A_z denotes the damped amplitude at depth z. This extended temperature function can be used to simulate the amplitude damping and phase shift for any arbitrary depth. The damping depth is the fundamental parameter for the propagation of periodic temperature oscillations into depth and is related to the thermal diffusivity ~~(~~α~~)~~ over the period length P:

$$d = \sqrt{\left(\frac{\alpha P}{\pi}\right)} \quad (5)$$

Eq. 5 shows that besides the thermal diffusivity α, the period length is determining the damping depth. The expected damping depth in the annual cycle is greater than in the daily cycle by a factor of $365^{0.5} = 19.1$. If the damping depth is known, the thermal diffusivity can be calculated by converting Eq. 5 as follows:

$$\alpha = \frac{\pi}{P} \cdot d^2 \tag{6}$$

When using temperature measurements at two or more depths, the damping depth can be derived from the phase shift (d_{phase}) and the amplitude damping ($d_{amplitude}$). In the ideal case of a harmonic temperature oscillation, d_{phase} equals $d_{amplitude}$. Both values can be obtained graphically by analyzing~~using~~ temperature measurements at a minimum of two depths (z_1, z_2), identifying~~defining~~ extreme values~~minimum and maximum~~ of the temperature waves and the time offset between~~of the~~ phases (t_1, t_2). For our analysis, the maximum of the temperature wave was chosen as the defining temporal marker. By multiplying the slope by the factor P/(2 π), d_{phase} can be calculated,

$$d_{phase} = \frac{P}{2\pi} \cdot \frac{(z_1 - z_2)}{(t_1 - t_2)} \tag{7}$$

while for the calculation of $d_{amplitude}$, the depth (z_1, z_2) is plotted against the natural logarithm of the amplitudes (A_{z1}, A_{z2}), with the slope equal to the value of $d_{amplitude}$:

$$d_{amplitude} = \frac{(z_1 - z_2)}{\ln(A_{z1}) - \ln(A_{z2})} \tag{8}$$

As the annual thaw process and its maximum depth for estimating active layer thickness (ALT) were ~~was~~ the focus of this study, the high-frequency daily temperature oscillations were neglected. A phase length of 365 days was assumed, resulting in a period length of 365 x 86400 s. Values for temperature at depth were calculated in a model via Eq. 4 with $\Delta z = 0.1$ m and $\Delta t = 24$ h. The chosen depth of 0.1 m, as a near-surface boundary condition, offers the advantage that temperature is undisturbed by turbulent heat flows on the ground surface. Furthermore, daily temperatures were smoothed with a moving average of five days. The year-specific mean temperatures in 0.1 m depth (T_m) were calculated using smoothed values. Therefore, the values of T_m differ minimally from the calculated mean annual ground temperature (MAGT) in 0.1 m depth which was calculated without curve smoothing. Ground temperatures and the annual thaw process in the summer are influenced by the previous winter (Dobinski, 2011). Therefore, the amplitudes were calculated based on half the difference in T_{min} and the T_{max} in the preceding summer months. Then t_m was determined as the day in each annual phase when $T_{(t,z)}$ first exceeded the value of T_m in the annual cycle. Since temperature oscillations at 0.1 m depth are very heterogeneous (even after smoothing), t_m was averaged from the six years investigated.

For model calibration (periods 2016 to 2018), the damping depth was adjusted ($d_{calibrated}$) to get the best match of the thawing process. For the model validation (periods 2019 to 2021), the values of daily thaw depths were tested using the Nash-Sutcliffe ~~e~~Efficiency ~~c~~Coefficient (NSE) (Nash and Sutcliffe, 1970). The NSE is a quality criterion for model efficiency of time series, and it penalizes deviations more severely for high values than for small values. The values of the NSE can range from negative infinity~~zero~~ to one, where one represents a perfect model fit. An NSE value greater than zero indicates that the model performs better than the mean of the observed data. In accordance with Hipp et al. (2012), for successful modeling, we assume a threshold value of > 0.7. After the maximum of the annual thaw depth, the model showed large deviations from the measured values in each of the six years, poorly representing the onset of the autumnal freezing process, which does not impact the modeling of the thawing process, which was the focus of our modeling approach.~~ and could thus poorly represent the beginning freezing process.~~ The modeled daily thaw depths were therefore only used to describe the thawing process and were modified on the day of maximum thaw depth by setting it to 0 m. The main emphasis of the model is not on the daily, but the annual max. thaw depths ~~to determine~~ (ALT), for which the temporal precision on a daily scale plays a minor role. Therefore, we assume a Root Mean Squared Error (RMSE) < 0.2 m between the measured and modeled ALT during the validation period for the modeling to be considered successful.~~ The modeled values of annual max. thaw depths (validation period) were tested with the NSE and the root mean squared error (RMSE).~~ The calculation of the damping depths from the phase shift over the annual temperature maxima (Eq. 7) and the amplitude damping (Eq. 8) helped to re-evaluate $d_{calibrated}$ to get a better interpretation of the model's robustness~~results~~.

To be able to apply the model to the SBs, a basic assumption was that the damping depth is identical to the calibrated damping depth ($d_{calibrated}$) determined at the DB, because the subsurface consisted of calcareous micaschist with highly similar properties at all locations. Climate projections were implemented by manipulating T_m following climate scenarios SSP1-2.6 and SSP5-8.5 (IPCC, 2023, Table SPM.1). When applying climate scenario SSP1-2.6, surface temperature is projected to increase by 1.6 °C and by 2.4 °C under SSP5-8.5 by mid-century (2041-2060), while by the end of the century (2081-2100), an increase of 1.8 °C is projected under scenario SSP1-2.6 and 4.4 °C under SSP5-8.5, respectively.

4. Results

4.1 Ground temperatures at the deep borehole

Temperature measurements at different profile depths are shown in Fig. 3a in the form of temperature oscillations of daily mean values. At 0.1 m depth, large overlaps of the annual temperature oscillations with the daily high-frequency temperature oscillations can be seen as pronounced noise. With increasing profile depth, the oscillations became more harmonic as short-term atmospheric temperature fluctuations lost influence. Each year, there was a short period of time at the onset of the autumnal freezing process~~beginning of the frost period~~, when temperatures dropped below 0 °C, during which ground temperatures cooled more slowly~~er~~ and, in some cases, remained nearly constant for a short time period (zero-curtain effect). The zero-curtain effect was strongest at 3 m depth. At a depth of 30 m, the effect of the annual oscillations on the subsurface temperatures became almost negligible since the annual oscillation amplitudes had been almost completely dampened. During the study period (2016–~~-~~2021), the annual mean temperature minimum and maximum at this depth were -1.78±0.04 °C and -1.75±0.05 °C, respectively, and the seasonal temperature variations were less than 0.1 °C, indicating that the zero-annual amplitude (ZAA) was reached (Williams and Smith, 1993). Table 3 provides ~~of~~ characteristic values of the temperature wave at 0.1 m depth. The temperature data interpolated over depth (z) are shown in Fig. 3b.

Table 3. Characteristic values of the annual temperature wave at 0.1 m depth at the north facing deep borehole (DB).

Year	T_{max}[1] (°C)	T_{min}[1] (°C)	Thaw index[1,2] (°Cd)	Frost index[1,2] (°Cd)	MAGT[1,3] (°C)	T_m[4] (°C)	As[5]
2016	9.54	-18.31	416	-1566	-3.14	-3.06	12.27
2017	9.99	-20.98	475	-1784	-3.55	-3.60	13.74
2018	9.04	-21.88	552	-1572	-2.79	-2.79	13.51
2019	13.08	-17.00	541	-1594	-2.88	-2.88	13.99
2020	8.46	-13.13	365	-1294	-2.57	-2.57	9.44
2021	10.75	-20.23	394	-1696	-3.58	-3.60	13.19
Mean	**10.14**	**-18.59**	**457**	**-1584**	**-3.09**	**-3.08**	**12.69**

[1]Values calculated without curve smoothing.

[2]The frost index is the temperature sum of all temperature values (daily averages) < 0 °C. Accordingly, the thaw index is the temperature sum of all temperature values (daily averages) > 0 °C.

[3]MAGT: mean annual ground temperature, calculated based on daily mean temperatures.

[4]T_m is the mean annual ground temperature used to drive the analytical model and calculated based on a five-day moving average of the daily mean temperature.

[5]A_s is the amplitude at 0.1 m depth used to drive the analytical model calculated from half the distance between the extreme values (T_{max} and T_{min}) of the annual temperature wave after curve smoothing (five-day moving average).

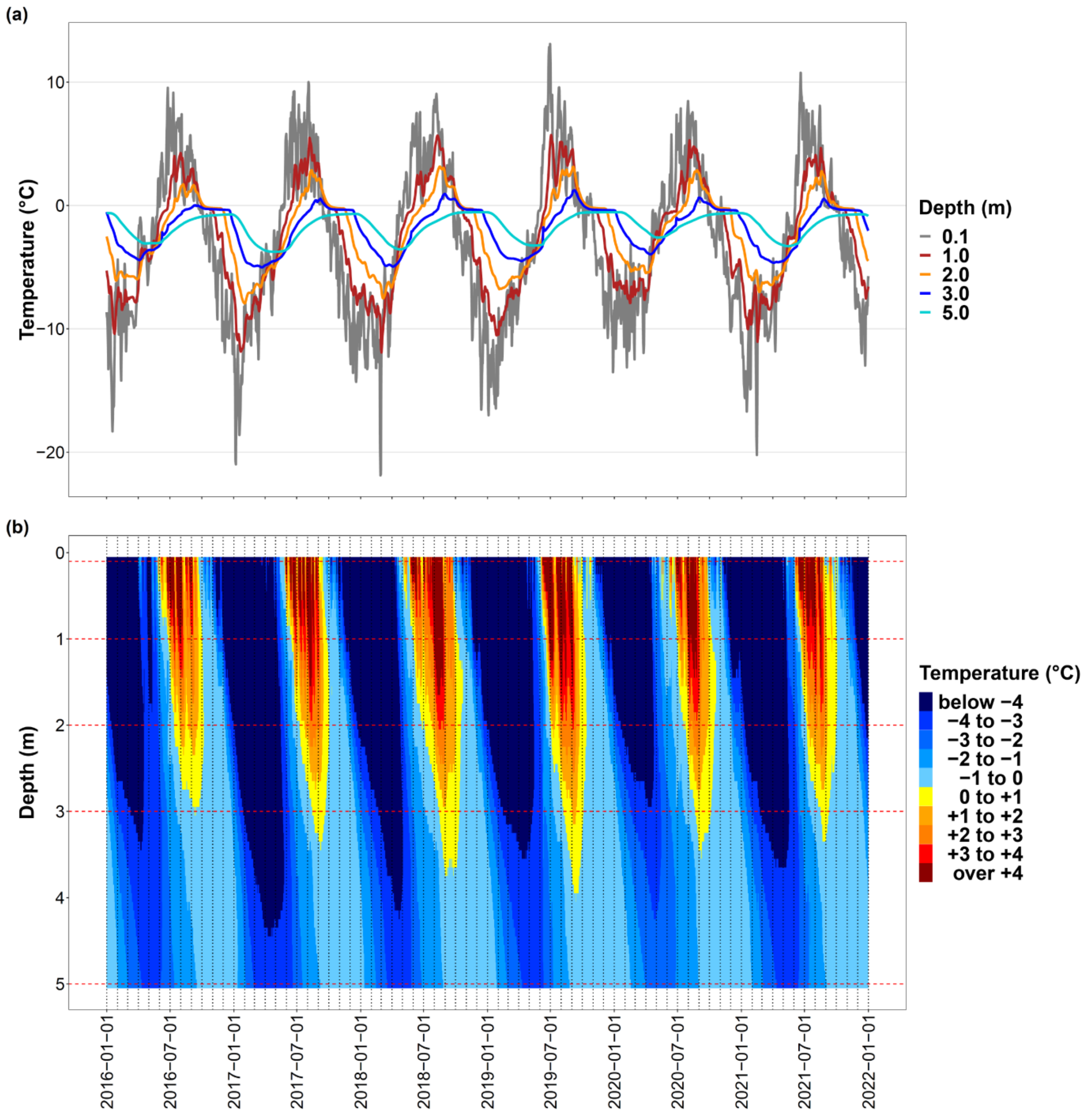

Figure 3: Temperature data and thawing process at the deep borehole (DB). (a) shows measured ground temperature (daily mean values) at different depths. (b) shows interpolated temperature data over depth and time (spline) as temperature classes. The red dashed cross lines refer to the depths at which temperature was measured (sensor depth).

285

Within the active layer, the mean annual ground temperature (MAGT) increased with depth (Fig. 4a). The mean thermal offset was 1.23±0.23 °C between 0.1 m and 3 m depth (within the active layer) and 1.42±0.29 °C between 0.1 m to 5 m depth. Accurate calculation of the damping depth from the phase shift (d_{phase}) was only possible for two years (2017 and 2018) and across three measurement depths, due to inharmonic temperature oscillations in the other years. As shown in Fig. 4b, the phase shift increased proportionally with depth, which is consistent with theory. In contrast, calculating the damping depth from the amplitude damping ($d_{amplitude}$) was possible for all years. Down to a depth of 3 m, the amplitude damping was rather homogeneous in depth (Fig. 4c). This indicates that thermal diffusivity was nearly constant down to that depth and that there were no significant depth-dependent differences (e.g., due to water saturation changes). It also indicates that amplitudes were exponentially more dampened with increasing depth, as expected from theory. Between 3 and 5 m depth, the amplitudes were less dampened due to a higher thermal diffusivity. Here, the thermal diffusivity $\alpha_{amplitude}$ calculated from amplitude damping was 0.89±0.22 x 10^{-6} m² s^{-1} on average over six years. For modeling the annual thaw process and ALT, the thermal diffusivity between 0.1 and 3 m (within the active layer) is more important.

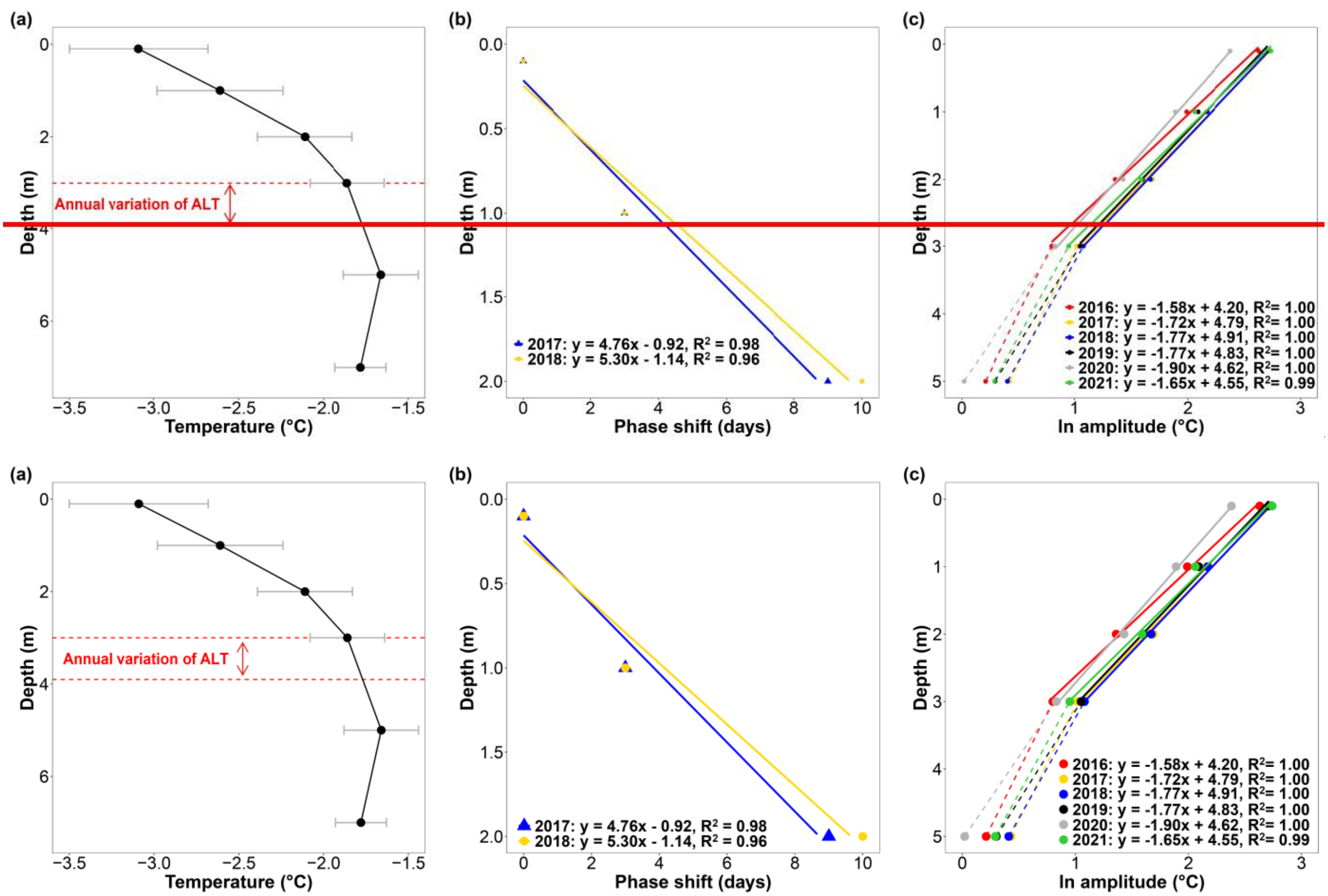

Figure 4: (a) ~~mean values of the m~~Mean annual ground temperature (MAGT) at different depths from 2016 to 2021. Due to sensor~~measurement~~ failure~~s~~, the data from 2020 and 2021 are missing at a depth of 7 m. The error bars show the standard deviation of the interannual variations. (b) ~~p~~Phase shift of the annual temperature wave with depth and the corresponding regression lines. Due to inharmonic oscillations, this could only be calculated over three depth levels and for only two years. (c) Damping of the annual temperature amplitude with depth, along with ~~and~~ the corresponding regression lines. Amplitude damping down to a depth of 3 m was highly consistent~~very homogeneous~~ (R^2 ≈ ~~close to~~ 1), which is critical in terms of magnitude for wave thermal propagation into the subsurface. The scattered lines show the amplitude damping between 3 m and 5 m depth (not included for calculating regression lines), i.e. within the permafrost. The amplitude damping between active layer and permafrost was lower than in the profile above.

Table 4 summarizes the estimated damping depths and calculated thermal diffusivities of the active layer, where the values of d_{phase} were larger than those of $d_{amplitude}$. Two basic theoretical assumptions for the analytical solution of the heat equation (Eq. 4) warranted a critical assessment, which is why the thermal diffusivities calculated via Eq. 6 ~~(Table 4)~~ could only be regarded as approximations: First, the MAGT was only constant to a rough approximation due to the thermal offset with depth. Second, the investigated temperature waves do not describe harmonic oscillations. This could already be seen in Fig. 3a and was further confirmed by the fact that d_{phase} was 0.97 m larger than $d_{amplitude}$. The damping depth calibrated via the modeling process ($d_{calibrated}$) was 2.4 m and thus lay within the interval of d_{phase} and $d_{amplitude}$ and relatively close to the mean value of d_{phase} and $d_{amplitude}$, which was 2.2 m.

Table 4. Damping depths from phase shift (d_{phase}) and amplitude damping ($d_{amplitude}$) and the corresponding calculated thermal diffusivities (α_{phase}, $\alpha_{amplitude}$).

Year	d_{phase} (m)	$d_{amplitude}$(m)	α_{phase} x 10^{-6} (m^2 s^{-1})	$\alpha_{amplitude}$ x 10^{-6} (m^2 s^{-1})
2016	(1.99)	1.58	(0.40)	0.25
2017	2.86	1.72	0.81	0.29
2018	2.54	1.77	0.64	0.31
2019	(4.65)	1.77	(2.15)	0.31
2020	(2.79)	1.90	(0.77)	0.36
2021	(6.97)	1.65	(4.84)	0.27
Mean	**2.70**	**1.73**	**0.73**	**0.30**

The values of d_{phase} without brackets were calculated between 0.1 and 2 m depth using linear regression over three depths (0.1, 1, 2 m). In contrast, the values of d_{phase} in brackets were only calculated over two depths (1–~~-~~2 m) without linear regression and were not included in the mean value calculation due to high uncertainty. The values of $d_{amplitude}$ were calculated using linear regression over four depths (0.1, 1, 2, 3 m). To calculate the thermal diffusivity α, a period length (P) of 365 days was assumed.

4.2 Modelling active layer thickness at the deep borehole

The thawing process was successfully modeled based on daily values. During the validation period, the Nash-Sutcliffe Efficiency Coefficient (NSE) was 0.79 (0.36 without model adjustment in the onset of the autumnal freezing period, see section

3.2), exceeding the required threshold of > 0.7 for successful modeling~~The daily thaw depths could be modeled satisfactory (NSE > 0.7)~~ (Fig. 5a and 5b). The main modeling focus was~~were~~ the annual values of~~max. thaw depth for determining~~ active layer thickness (ALT). In 2016 (calibration period), the model showed the largest deviation from the measured value (Fig. 5a). In that year, the surface penetrating amplitude was also damped the most (Fig. 4c) and $\alpha_{amplitude}$ was consequently the smallest (Table 4). For the remaining years, ALT~~annual max. thaw depths~~ could be modeled with satisfactory accuracy over the entire study period. In the validation period (three data pairs), the RMSE was 0.13 m,~~ the NSE was 0.76, ~~ well below the required maximum threshold (< 0.2 m), indicating successful modeling, ~~which was well above the required threshold of 0.7 ~~and a close match between measured and modeled ALT-values~~ the modeled ALT was very close~~ (Fig. 5c).

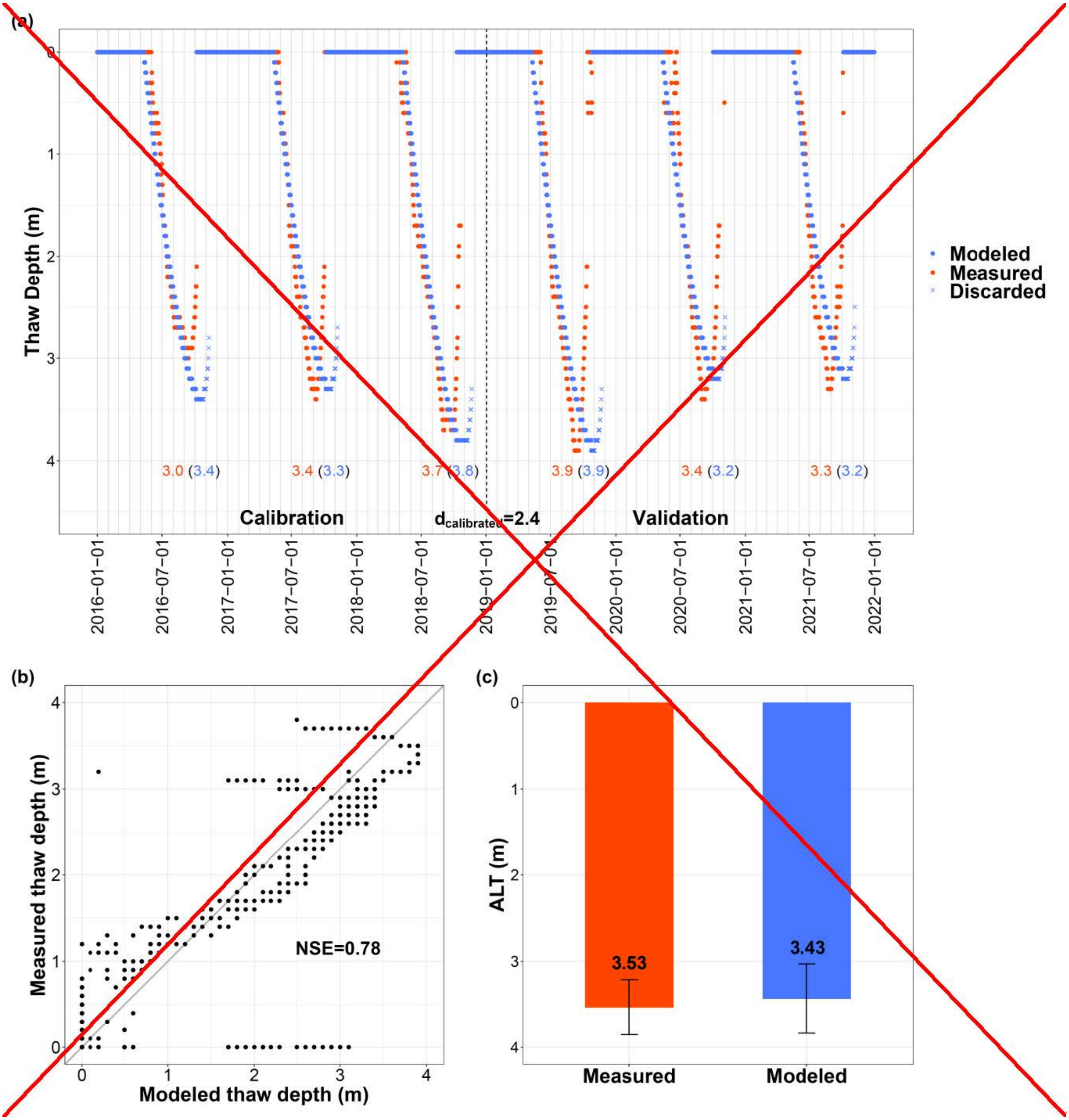
(a)
Thaw Depth (m)
Modeled
Measured
Discarded
3.0 (3.4)
3.4 (3.3)
3.7 (3.8)
3.9 (3.9)
3.4 (3.2)
3.3 (3.2)
Calibration
$d_{calibrated}$=2.4
Validation
2016-01-01
2016-07-01
2017-01-01
2017-07-01
2018-01-01
2018-07-01
2019-01-01
2019-07-01
2020-01-01
2020-07-01
2021-01-01
2021-07-01
2022-01-01
(b)
Measured thaw depth (m)
NSE=0.78
Modeled thaw depth (m)
(c)
ALT (m)
3.53
3.43
Measured
Modeled

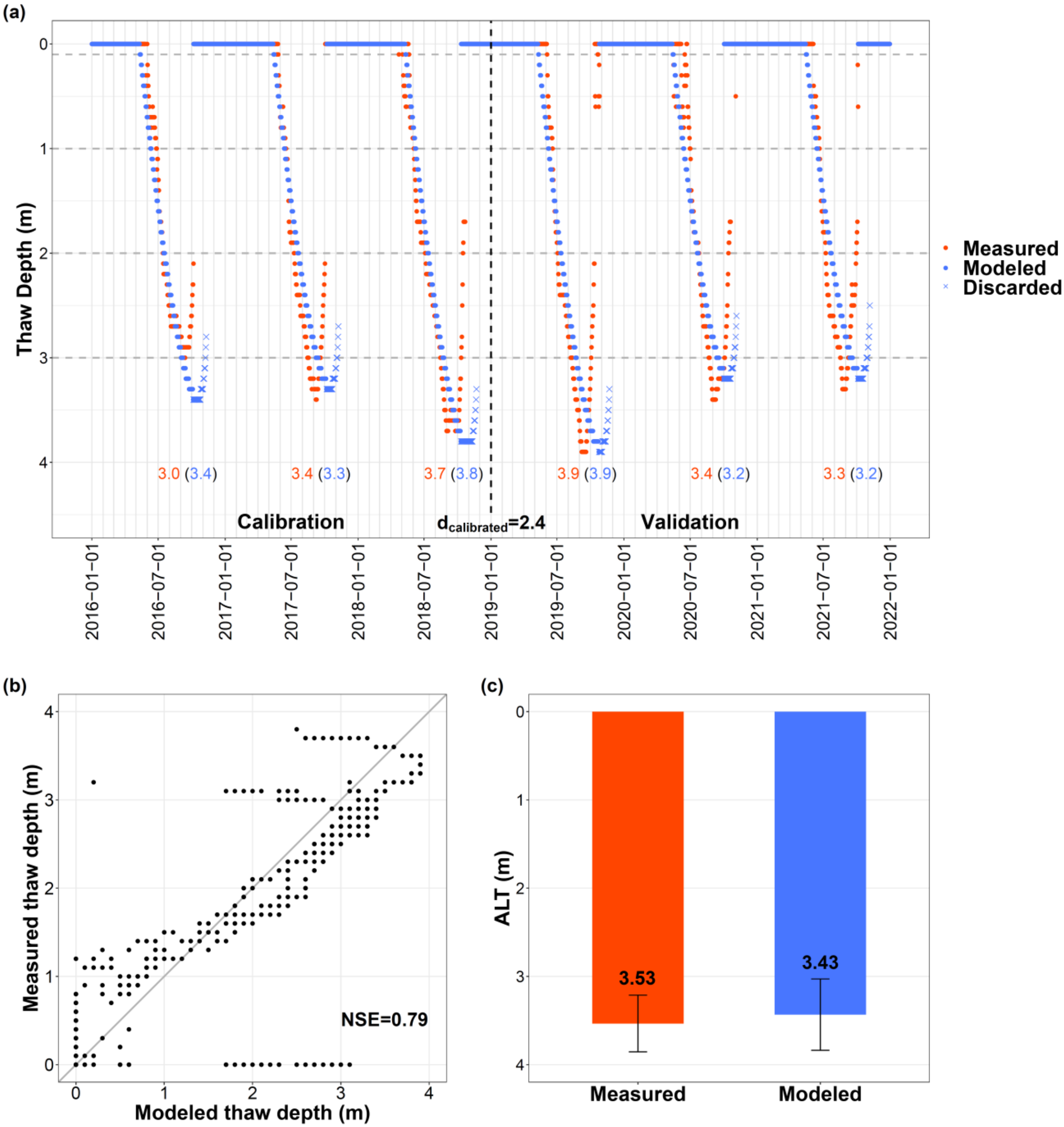

Figure 5: (a) Daily measured and modeled thaw depths at the deep borehole (DB).~~ The given numbers represent the annual maximum thaw depth.~~ The calibrated damping depth ($d_{calibrated}$) expresses the thermal diffusivity for thermal wave propagation with depth. The onset of the autumnal frost process could not be represented well, so modeled values for the time after the annual thaw depth maximum were discarded and replaced by the value zero. The red (measured) and blue (modeled) numbers represent the annual values of the active layer thickness (ALT). The dashed horizontal lines indicate the depths at which temperature was measured (sensor depth). (b) Scatterplot of daily measured and modeled thaw depths for the validation period; gray line = line of

equality; NSE=Nash-Sutcliffe ~~e~~Efficiency ~~c~~Coefficient. (c) Mean values of the measured and modeled ~~active layer thickness (~~ALT~~)~~ of the validation period; the error bars show the standard deviation.

4.3 Spatial and future projection of active layer thickness

Table 5 shows ALT values for the studied deep borehole (DB) and the four shallow boreholes (SBs). The west- (SB 1), east- (SB 3), and south-facing (SB 4) boreholes (Table 2) were the warmest (Appendix B). At SB 3, five out of seven modelled years showed a positive MAGT calculated with a sliding average for analytical modelling (T_m, see section 3.2); no ~~two~~ consecutive years with a negative T_m were found. This indicates that permafrost was not present there. Permafrost was present at SB 1 and SB 4, but one year with a positive T_m was also observed at each of the two sites. In contrast to SB 1 and SB 4, which had similarly high ALT values, the two north-facing boreholes (DB and SB 2) showed a much smaller ALT. In direct comparison, the ALT at SB 2 was 0.5±0.2 smaller than at DB (average of 2016 to 2019).

It has to be noted that the model results do not reflect potential lateral heat flow between SB sites. In reality, such heat flows would certainly occur between the closely grouped trio SB 2–4, which would significantly reduce the high ALT variability between the sites. Modeled ALT values therefore should be interpreted as idealized representations of their respective slope aspect not affected by 3D topography effects.

Table 5. Measured (deep borehole = DB) and modeled (shallow borehole = SB) values of the annual maximum thaw depths in m.

Year	DB	SB 1	SB 2	SB 3	SB 4
2013	-	6.3	2.7	-	7.2
2014	-	5.1	-	NP	5.1
2015	-	6.9	-	10.4	9.4
2016	3.0	8.1	2.5	NP	-
2017	3.4	6.8	3.1	6.8	-
2018	3.7	10.6	3.3	NP	10.3
2019	3.9	NP	3.1	NP	NP
2020	3.4	8.2	-	NP	8.4
2021	3.3	6.8	-	-	5.8

NP = no permafrost, (-) indicates data gaps due to measurement failures.

Following SSP1-2.6, permafrost will no longer be present at SB 1, SB 3, and SB 4 by mid-century after an increase in T_m. Projections of the future ALT could only be made for the coldest north-exposed boreholes DB and SB 2 (Fig. 6). Towards mid-century, the model showed an increase in the ALT of 48 % under SSP1-2.6 and 76 % under SSP5-8.5. Towards the end of the century, permafrost at SB 2 can only be expected under scenario SSP1-2.6 with an ALT increase of 51 %. At the slightly warmer DB, the model showed a 62 % increase in the ALT under SSP1-2.6 and a 128 % increase under SSP5-8.5 toward mid-century. Toward the end of the century, permafrost at DB can only be expected under scenario SSP1-2.6 with a 69 % increase in the ALT.

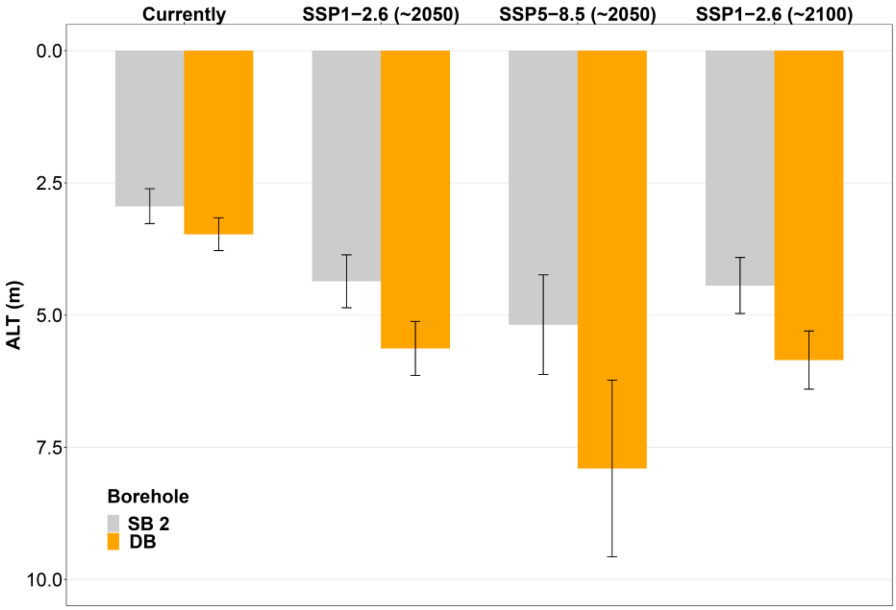

Figure 6: Projections of future ALT assuming scenarios SSP1-2.6 and SSP5-8.5 at the mid and end of the century at the deep borehole (DB) and shallow borehole 2 (SB 2). Towards the end of the century, permafrost can only be expected to occur in these two coldest, north-facing boreholes under scenario SSP1-2.6. The current ALT was calculated on the basis of all measured values during the study period, whereby the years included in the calculation were different in some cases (see Table 5). The colored bars show the mean values, the error bars the standard deviation.

5. Discussion

5.1 Ground temperatures at the deep borehole

~~The m~~Mean annual ground temperature (MAGT) rises with increasing depth within the active layer. This positive thermal offset of the MAGT with depth is surprising. An opposite (negative) thermal offset is a well-known phenomenon in polar regions (Burn and Smith, 1988; Romanovsky and Osterkamp, 1995; Smith and Riseborough, 2002) and was also already detected in mountain (bedrock) permafrost (Hasler et al., 2011), usually caused by a seasonal variation of the water saturation and its phase changes in the subsurface (Gruber and Haeberli, 2007). These variations cause the cooling front to usually penetrate the profile more deeply than the heating front resulting in a negative thermal offset. However, Hasler et al. (2011) also observed a positive thermal offset within the active layer for one out of nine temperature observations in mountain (bedrock) permafrost.

At the deep borehole (DB), the positive thermal offset was likely caused by (i) convective~~advectiv~~ heat flow due to significant subsurface meltwater flow during the thaw period, combined with (ii) an increase in thermal diffusivity due to increased water saturation with depth: ~~During~~ At the onset of each~~the~~ thaw season (around ~~∼~~June), we observed ~~sudden,~~ sharp, small temperature jumps at 2, 3~~ m~~ and 5 m depth, typically by a few tenths of a degree. These abrupt changes ~~, which~~ can only be ~~explained by~~ attributed to fluid heat flow (convection) in joints~~fractures~~ ~~(~~and not by conduction-driven warming~~)~~. This observation is consistent with optical scan data from the deep borehole (DB), which demonstrates open, surface-parallel (~ 45°) joints along the natural schistosity of the bedrock (calcareous mica-schist) that form ideal pathways for subsurface lateral water flow. Recent geoelectrical and piezometric measurements from the Kitzsteinhorn confirm these assumptions and demonstrate the temporary presence of liquid subsurface water (Offer et al., accepted). In addition, the zero-curtain effect observed in the measured temperature waves, which is caused by release~~ and consumption~~ of latent heat during the phase change from~~of~~ water to ~~/~~ice (Outcalt et al., 1990), became more pronounced with increasing depth and was strongest~~especially strong~~ at 3 m depth within the active layer. At the end of the thaw period, water saturation at depth was therefore increased.

Depth-dependent damping of annual amplitudes was remarkable ~~very~~ homogeneous, and consequently, no large changes are to be expected for vertical heat transport over the depth range studied. However, this refers to the damping of annual amplitudes and therefore does not necessarily exclude temporary water flow,~~ –~~ which likely is responsible for the observed thermal offset. Within the permafrost body, i.e., below the active layer, amplitude damping was less pronounced. This is most likely related to the phase change of joint and pore~~fissure~~ water, since ice has a thermal diffusivity roughly five (James, 1968) to eight times (Oke, 1987; Garratt, 1994) higher than liquid water.

5.2 Modelling active layer thickness at the deep borehole

We successfully modeled active layer thickness ~~the~~ (ALT) with an analytical solution of the heat transport equation based on near-surface temperature data (0.1 m depth). The accuracy of the modeled ALT was satisfactory. During the validation period (three data pairs, 2019–2021), the Root Mean Square Error (RMSE) is 0.13 m, well below the required threshold (< 0.2 m, see section 3.2), indicating successful modeling. ~~, modeled and measured values of ALT differed by only 0.1±0.1 m during the validation period, with a Nash-Sutcliffe efficiency coefficient (NSE) value of 0.76, which was well above the threshold of 0.7 required for successful modeling (see section 3.2).~~ The largest deviation between measured and modeled ALT was observed for 2016 (calibration period), with a value of 0.4 m. In that year, the surface penetrating temperature amplitudes were damped the most, and the calculated thermal diffusivity ($\alpha_{amplitude}$) was the smallest during the study period. In line with that, the largest differences between the calibrated damping depth ($d_{calibrated}$) and the damping depth calculated from amplitude damping ($d_{amplitude}$) were also observed in 2016. No significant structural changes are expected in the bedrock of the calcareous mica-schist over the study period. Therefore, it is reasonable that a lower joint and pore water content decreased thermal conductivity (Kim and Oh, 2019) and thus $\alpha_{amplitude}$, and as a result caused the largest model deviations in that year. The thawing process was successfully represented based on daily values, with a Nash-Sutcliffe Efficiency Coefficient (NSE) of 0.79, which is well above the required threshold (> 0.7, see section 3.2), further demonstrating the model's reliability. In contrast, the onset of autumnal active layer freezing was not well represented, likely due to the model's inability to account for an altered thermal conductivity during phase changes.

While joint and pore water certainly had some influence (thermal offset and a zero-curtain effect within the active layer), the combined evidence from the (i) remarkable homogeneous damping of temperature amplitudes with depth (Fig. 4c), (ii) smooth temperature change over time and depth without abrupt jumps (apart from small temperature jumps at 2–5 m depth at the onset of each thaw season), and (iii) excellent model results from a model approach that is exclusively conduction-based clearly indicates that conduction is the dominant heat transfer mechanism for local ALT formation. Laboratory tests of local calcareous mica schist core samples demonstrate an effective porosity of only 0.3–0.4 % (see section 2 and Appendix C). Based on this low porosity we assume that the effect of latent heat transport is only marginal and has no significant effect on ALT formation, which thus supports the validity of excluding latent heat effects from our model.

For the application of the analytical solution of the heat transport equation, two basic assumptions ~~have to~~must be considered critically: First, the MAGT was not constant ~~at~~ with depth (z) or was constant only as a very rough approximation. Second, the annual temperature waves did not describe harmonic oscillations. Temporal variability of weather conditions is the main reason for the deviation of annual air and ground temperature oscillations from an ideal sinusoidal pattern (Rajeev and Kodikara, 2016). Nevertheless, the good calibration and validation possibilities at DB permitted a relatively robust estimation of the calibrated damping depth ($d_{calibrated}$) ~~for the vertical heat transport~~. In ideal harmonic oscillations, the values of ~~d_{phase} and~~ $d_{amplitude}$ and the damping depth derived from phase shift (d_{phase}) are approximately equal. This was not the case in our study;~~,~~ however, ~~the calibrated damping depth~~ $d_{calibrated}$ (2.2 m) fell within the range~~was in the interval~~ of d_{phase} and $d_{amplitude}$ and was relatively close to their mean value ~~of d_{phase} and $d_{amplitude}$~~ (2.4 m). This indicates a high plausibility that $d_{calibrated}$ can physically describe the vertical conductive heat transport for modeling the thawing process. ~~Via an analytical solution of the heat transport equation, the local thermoregime can be representatively captured. The idealized forcing of the model provides the basis for performing relatively simple scenario-based future projections based on the manipulation of the surface temperature as boundary condition.~~

5.3 Spatial and future projection

Following model development with data from the DB, we applied the model to the shallow boreholes (SBs) and integrated IPCC climate scenarios for future ALT simulations. The chosen depth of 0.1 m, as a near-surface boundary condition, offers the advantage that temperature is undisturbed by turbulent heat flows on the ground surface — furthermore, this depth inherently accounts for the effect of any potential snow cover. Our modeling approach did not take into account topography-induced 3D effects on the ALT, instead we considered the SBs as idealized representatives of their slope aspect, which are not affected by lateral subsurface heat flow from other sides of the summit pyramid. Due to the study area's uniform lithology, we furthermore assumed that thermal properties at the SBs did not significantly differ from the ~~in thermal properties at the~~ DB, and that $d_{calibrated}$ can be transferred to the SBs. ~~Minor spatial variations of the thermal properties may still introduce uncertainty into the model application at the SBs, however, our modeling approach offers the advantage that the spatial variability of the local thermal regime is excluded and the actual influence of topographic factors can be better captured. Thus, ALT can be estimated on a larger spatial scale, and subsequently, conclusions can be drawn about rock and slope stability.~~

In the study area, slope aspect is the dominant topographic factor influencing ALT due to ~~low~~ small elevation differences between the investigated boreholes (~ 200 vertical meters). As a result, the smallest ALT (2.5–~~-~~3.9 m) was found at the two north-facing boreholes DB and SB 2, which are both characterized by clear permafrost conditions. Large ALT values between five and ten meters were found at SB 1 and SB 4. Under current climatic conditions no permafrost is indicated for SB 3, the subsurface, however, could still contain relict permafrost produced by cooler conditions in the past. Somewhat surprisingly, apart from 2019, the south-facing borehole SB 4 is slightly colder (T_m, Table B1) and thus has a higher permafrost probability than the east-facing borehole SB 3. This is most likely related to differences in rockwall gradients and their impact on ~~the~~ local, small-scale snow cover patterns. The south-facing borehole SB 4 is located in a moderately steep rockwall section that hosts a small, thick snowpack during winter, spring and early summer. While this insulation efficiently prevents the propagation of cold winter temperatures into the subsurface (warming effect), it also leads to a significant delay of seasonal warming (cooling effect) as compared to the east-facing SB 3, which is exposed to direct sunlight the entire year and, due to its steep gradient (~ 80°), absorbs significant amounts of solar radiation even at low sun angles (winter season).

While slope aspect has been demonstrated here as a key factor for ALT evolution, this example illustrates that the topo-climatic disposition (slope aspect, slope gradient, elevation, topographic shading) can potentially be altered by local snow cover effects. The discussed influence of slope aspect is therefore straightforward only under the assumption of a uniform snow cover regime. Here, it is important to add that small-scale (~ a few m²) snow cover effects have a pronounced influence on ALT model results, due to their dependence on temperature measurements carried out just 0.1 m below the rock surface. Consequently, our approach overestimates ALT sensitivity to small-scale snow cover variations, as the real seasonal ALT values results from thermal forcing over larger areas. This case emphasizes the significance of selecting representative sites for SB measurement and demonstrates the challenge of reconciling processes across different spatial scales.

ALT projection under scenario SSP5-8.5 suggests that, by mid-century, mountain permafrost will only be present at the north-facing boreholes, with a significant increase in ~~and that~~ ALT ~~will increase considerably~~. Toward the end of the century, however, permafrost is expected to disappear entirely, ~~will no longer be encountered also~~ even at these two coldest boreholes under this scenario. However, uncertainties in the future projection exist, particularly related to future snow cover patterns and the insulating properties of the snow cover, which leads to seasonal decoupling of atmospheric and ground surface temperatures. Despite these uncertainties, a key~~A~~ conclusion transferable from this projection to other permafrost regions is that a larger initial ALT (DB: 2.9 compared to SB 2: 3.5) will also lead to~~result in~~ a larger increase in ALT for the same temperature rise~~increase~~ (regarding to SSP5-8.5 for mid-century, SB 2: 56%, DB: 128%). This shows that in warm permafrost, even small changes in temperature cause large increases~~changes~~ in ALT, which has significant implications for rock and slope stability. Study results from the Western Alps point to increased rockfall activity along the lower permafrost boundary, i.e. in regions with (already) large ALT. Rockfall documentations from Switzerland demonstrate a late-summer peak in rockfall activity in regions with warm permafrost around 3,000 m a.s.l. (Kenner and Phillips, 2017) and analyses of a century-long inventory of slope failures from the central European Alps (France, Italy, Switzerland) indicate increased mass wasting in low-lying permafrost regions (Fischer et al., 2012). As global~~climate~~ warming is expected to continue or even accelerate, this trend will most likely be reinforced over the next decades. Warming-induced upward migration of the lower permafrost boundary may result in a slight altitudinal shift of rockfall activity, while active layer thickening will most likely activate deeper failure planes and cause larger rockfall volumes – and will require significantly deeper foundations for constructions on permafrost.

5.4 Application potentials of analytical ALT modeling

Despite limitations in accurately modeling ground temperature on a daily scale due to the neglection of latent heat, convection, and altered thermal conductivities during phase changes, our approach demonstrates for the first time, that ALT in steep bedrock environments can be effectively modeled using a simple, time- and cost-efficient method. The chosen analytical solution to the heat conduction equation adequately captures the local thermoregime and overcomes the constraints of numerical models in terms of accuracy when relying on a limited number of field measurement points, computational costs for simulation runs and reliable parameter optimization and identification. Unlike numerical approaches, our method allows for straightforward and fast predictions of ALT under varying boundary conditions (idealized model forcing) without requiring expertise in numerical modelling. Estimating ALT based on near-surface bedrock temperature, combined with analytical modeling, thus offers a practical and powerful tool that could be integrated into expert systems for bedrock permafrost regions. As the study area does not exhibit highly specific site conditions that would distinguish it from other steep bedrock environments, our findings are likely applicable to other active layers in predominantly conduction-driven systems (bedrock). Due to the widespread availability of near-surface bedrock temperature data, our ALT model approach can be readily applied at numerous other high-alpine sites with adequate temperature datasets and similar boundary conditions.

Low computational demands, along with the absence of complex and highly site-specific calibrations, furthermore hold the theoretical potential for large-scale application, e.g. at the scale-level of an entire mountain range. This would, in a first step, require the development of a near-surface bedrock temperature model, for example following an empirical-statistical approach based on key topographic parameters verified by local bedrock temperature data. Using such a model, large-scale estimations of ALT could be performed, akin to previous studies that employed similar approaches to model the probability of permafrost occurrence (Schrott et al. 2012). While an ALT model of this type would involve considerable inaccuracies related to the modification of the ALT through snow cover dynamics and 3D topography effects, it could serve as a valuable tool for quantitative permafrost and natural hazard assessment in complex, high-alpine terrain.

6. Conclusions

~~The active layer thickness (ALT) of a permafrost body and its evolution over time is highly sensitive to climatic changes and of direct relevance in many important fields such as natural hazard analysis, construction, land-use planning and greenhouse gas emission studies.~~

The active layer thickness (ALT) in mountain permafrost, an increasingly critical factor for natural hazard management, is particularly responsive to climate change. This is especially true for steep permafrost rockwalls, which are highly sensitive to air temperature fluctuations due to their typically thin snow cover and low subsurface ice content (limited pore volume), which reduces the delaying effect of latent heat processes. In the present study, we used borehole temperature data from the summit region of the Kitzsteinhorn (Central Eastern Alps, Austria) to model ~~the annual maximum~~ ~~thaw depths for~~ ALT ~~analyses~~. We draw the following conclusions:

- To model ALT, we analytically solved the heat transport equation through sinusoidal thermal waves which propagate into the subsurface. A six-year dataset from a 30 m deep bedrock borehole was used for model calibration and validation. So far, simulations of the ALT (bedrock permafrost) were based on numerical models, the present study reports the first analytical solution to the heat transport equation to model ALT in ~~mountain~~ permafrost rockwalls (borehole scale) and offers a concise, process-based understanding how (modified) input parameters impact the studied system.
- Measured and modeled ALT values were highly consistent: During the validation period (2019–~~-~~2021), modeled and measured ALT at the deep borehole (DB) differed by only 0.1±0.1 m, with a Root Mean Square Error (RMSE) of 0.13 m, well below the required maximum threshold (< 0.2 m), indicating successful modeling. Additionally, the thawing process was accurately represented based on daily values, with a Nash-Sutcliffe Efficiency Coefficient (NSE) of 0.79, which is well above the required threshold (> 0.7), further demonstrating the model's reliability. ~~The Nash-Sutcliffe efficiency coefficient (NSE) equaled 0.76 and therefore was well above the threshold of 0.7 required for successful modeling.~~
- We used the developed thermal model to simulate ALT at four shallow boreholes (SBs, 0.1 m deep)~~,~~ located in close proximity~~in the immediate vicinity~~ and found that the modeled ~~seasonal maximum of the~~ ALT ranged between 2.5 m (SB 2) and 10.6 m (SB 1) in the observation period (2013–~~-~~2021). Due to small differences in altitude (~ 200 m) within the study area, slope aspect had the strongest impact on the ALT; however, this effect can potentially be modified by snow cover effects.
- Under the more moderate SSP1-2.6 scenario by mid-century, ALT is expected to increase by 48 % at SB 2 and by 62 % at DB, while permafrost will no longer exist at SB 1, SB 3 and SB 4.
- The impact of a temperature increase on ALT is more pronounced when the~~The effect of an increase in temperature on ALT is enhanced by a higher~~ initial ALT is higher. This suggests~~indicates~~ that in warm permafrost, even small rises~~changes~~ in temperature can lead to substantial increases ~~cause large changes~~ in ALT, which has significant implications for rock and slope stability.
- In contrast to permafrost soils, which have higher porosity and water content, latent heat appears to play a secondary role in the annual ALT evolution of bedrock permafrost with very low pore volumes. This condition makes the use of this relatively simple model approach possible.

- With its mathematical simplicity, lack of complex parameterization, and the widespread availability of near surface temperature data, our model approach is directly applicable to a wide range of other steep bedrock sites. By incorporating topography-based estimates of near-surface ground temperatures, ALT could be modelled at larger spatial scales in the future. Integrating latent heat exchange and altered thermal conductivities through phase changes and the effects of advective heat transport in joint and pore water could be useful improvements of the presented analytical modelling approach especially for higher porous media and wet conditions where latent heat flow may play a more prominent role.

Appendix A: Measured and interpolated temperature data at the deep borehole.

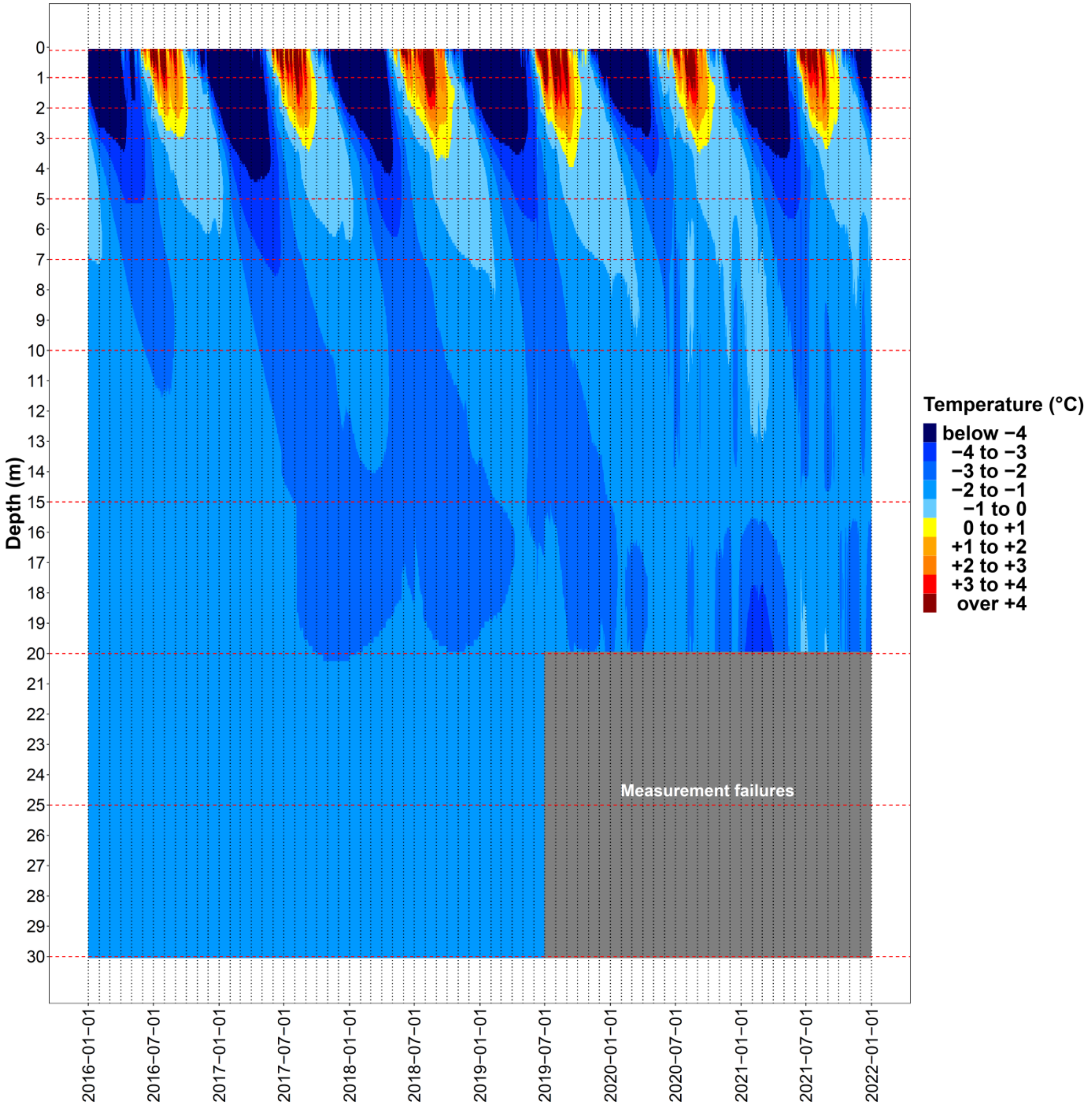

560 **Figure A1: Interpolated temperature data over depth and time (spline) as temperature classes. The red dashed cross lines refer to the depths at which temperature was measured (sensor depth). In the gray filled area, the values could not be displayed accurately due to measurement gaps. The temperature sensor at 7 m depth has also failed since 14.06.2020, which is why the interpolation values between 5 and 10 m may be less precise from then on.**

Appendix B: Yearly trumpet diagrams for the deep borehole.

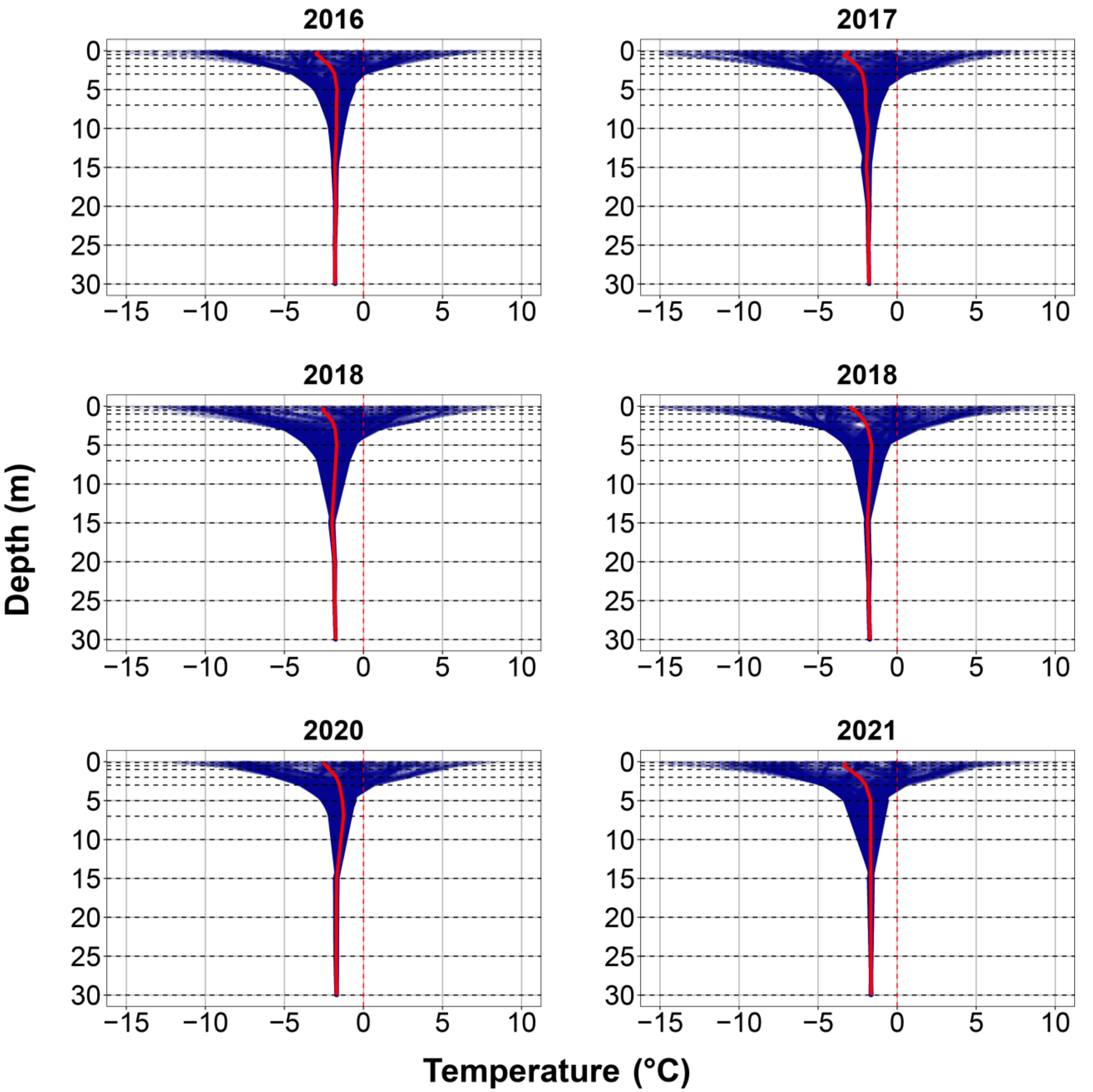

Figure A2: Yearly trumpet diagrams (depth vs. temperature) for the deep borehole (DB) based on daily mean temperature (2016–2021). Sensor depths are indicated by dotted horizontal lines. Temperature values between sensor depths is derived from linear interpolation. Solid, red line represents annual mean temperature.

Appendix B: Temperature data at the four shallow boreholes.

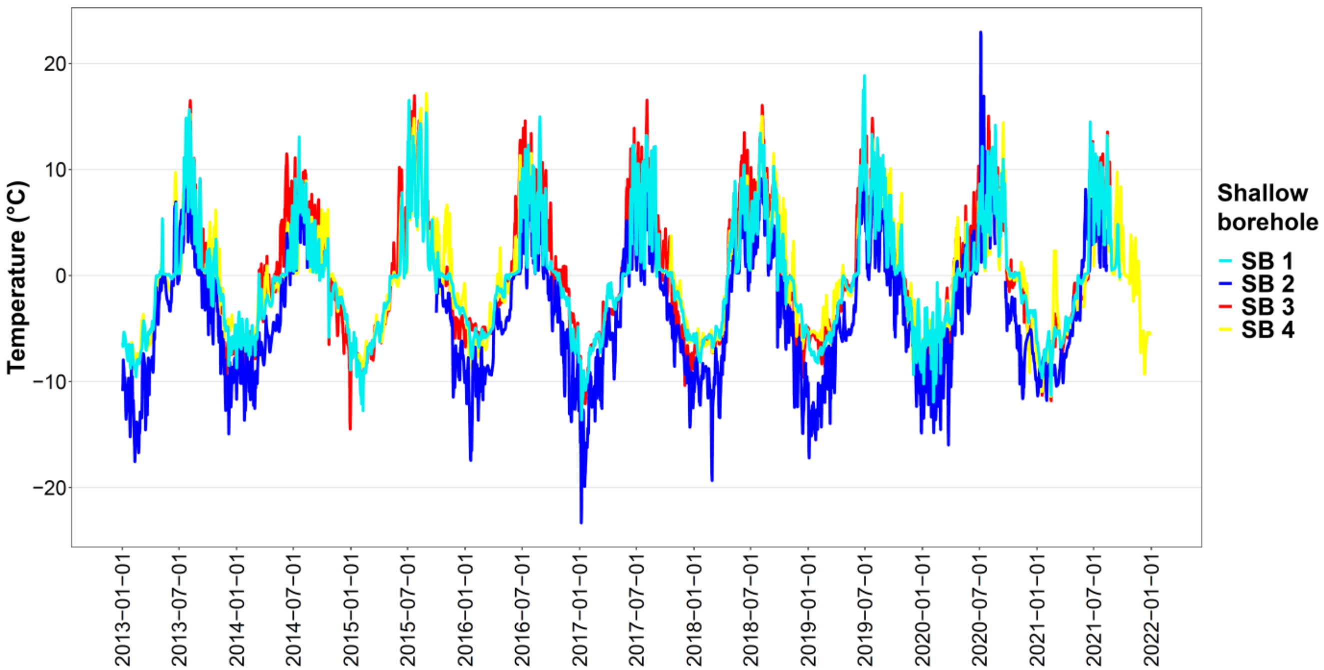

Figure B1: Measured ground temperature (daily mean values) at the investigated shallow boreholes (SBs). In some cases, there were large gaps in the data, in which case the temperature lines are shown as interrupted.

Table B1. Values for the analytical modeling, calculated from the temperature wave at a depth of 0.1 m in °C.

Year	SB 1		SB 2		SB 3		SB 4	
	T_m	A_s	T_m	A_s	T_m	A_s	T_m	A_s
2013	-0.88	11.91	-4.24	12.50			-0.58	11.32
2014	-1.02	8.24	-	-	0.01	11.18	-0.90	7.42
2015	-0.73	12.73	-	-	-0.18	13.37	-0.25	11.99
2016	-0.36	10.43	-4,10	11.40	0.33	9.64	-	-
2017	-0.77	12.56	-3,99	14.38	-0.79	13.13	-	-
2018	-0.12	10.10	-3,33	12.65	0.56	11.47	-0.16	11.02
2019	0.13	12.57	-3,63	12.77	0.09	13.06	0.64	11.12
2020	-0.34	10.22	-	-	0.22	11.48	-0.28	9.00
2021	-0.66	11.12	-	-	-	-	-1.04	-1.04

The temperature wave (daily averaged temperatures) was smoothed with a moving average of five days. T_m is the mean annual ground temperature and A_s is the temperature amplitude calculated from half the distance between the extreme values (T_{max} and T_{min}) of the annual temperature wave. Both model parameters served as surface boundary conditions for analytical modeling.

Appendix C: Determination of porosity values on local core samples.

Table C1: Characteristics and physical properties of calcareous mica-schist core samples.

	K1-1	K1-2	K2-1	K2-2	K3-1	K3-2	K4-1
Length (mm)	100.8	116.3	99.1	106.1	107.0	92.2	82.3
Diameter (mm)	54.6	54.6	54.6	54.7	49.6	49.6	54.7
Volume (cm³)	236.1	272.3	231.7	249.4	206.4	177.9	193.6
Matrix volume V_m (cm³)	234.7	270.3	230.6	247.5	204.6	176.1	192.3
Pore volume (cm³)	1.36	2.01	1.03	1.94	1.81	1.82	1.29
Effective porosity ϕ_{eff} (%)	0.3	0.3	0.3	0.3	0.3	0.4	0.4
Porosity ϕ (%)	0.6	0.7	0.4	0.8	0.9	1.0	0.7

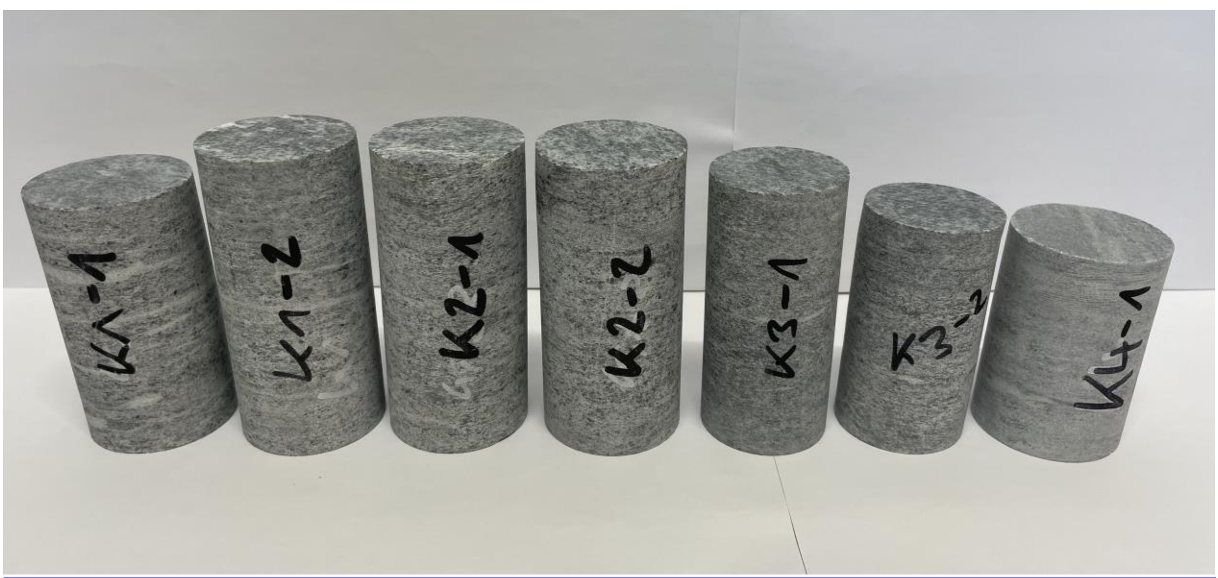

Figure C1: Photograph of seven calcareous mica-schist cores used for porosity tests (photo taken by M. Offer).

Data availability

The data that support the findings of this study are openly available in the repository Zenodo at https://doi.org/10.5281/zenodo.10203390 (Aumer and Hartmeyer, 2023).

Competing interests

We have no competing interests to declare.

Author contributions

WA took the lead in writing the manuscript with support from IH, CMG, DU, MO and SP. IH provided the temperature data while WA derived the models and analysed the data. MO contributed the core sample data. All authors contributed to the manuscript revision and approved the final version.

Acknowledgements

We would like to thank the Gletscherbahnen Kaprun AG (project “Open-Air-Lab Kitzsteinhorn”) and the Austrian Research Promotion Agency (FFG) (project “MOREXPERT”). Furthermore, we acknowledge support by the Open Access Publishing Fund of Geisenheim University. Many thanks to Claudia Kammann for valuable advice and final proofreading.

References

Allen, S. and Huggel, C.: Extremely warm temperatures as a potential cause of recent high mountain rockfall, Global and Planetary Change, 107, 59–69, https://doi.org/10.1016/j.gloplacha.2013.04.007, 2013.

Aumer, W. and Hartmeyer, I.: Borehole temperatures and thaw depths in mountain permafrost, Kitzsteinhom, Hohe Tauern Range, Austria [Data set], Zenodo, https://doi.org/10.5281/zenodo.10203390, 2023.

Balkan, E., Erkan, K., and Şalk, M.: Thermal conductivity of major rock types in western and central Anatolia regions, Turkey, Journal of Geophysics and Engineering, 14, 909–919, https://doi.org/10.1088/1742-2140/aa5831, 2017.

Biskaborn, B. K., Lanckman, J.-P., Lantuit, H., Elger, K., Streletskiy, D. A., Cable, W. L., and Romanovsky, V. E.: The new database of the Global Terrestrial Network for Permafrost (GTN-P), Earth Syst. Sci. Data, 7, 245–259, https://doi.org/10.5194/essd-7-245-2015, 2015.

Biskaborn, B. K., Smith, S. L., Noetzli, J., Matthes, H., Vieira, G., Streletskiy, D. A., Schoeneich, P., Romanovsky, V. E., Lewkowicz, A. G., Abramov, A., Allard, M., Boike, J., Cable, W. L., Christiansen, H. H., Delaloye, R., Diekmann, B., Drozdov, D., Etzelmüller, B., Grosse, G., Guglielmin, M., Ingeman-Nielsen, T., Isaksen, K., Ishikawa, M., Johansson, M., Johannsson, H., Joo, A., Kaverin, D., Kholodov, A., Konstantinov, P., Kröger, T., Lambiel, C., Lanckman, J.-P., Luo, D., Malkova, G., Meiklejohn, I., Moskalenko, N., Oliva, M., Phillips, M., Ramos, M., Sannel, A. B. K., Sergeev, D., Seybold, C., Skryabin, P., Vasiliev, A., Wu, Q., Yoshikawa, K., Zheleznyak, M., and Lantuit, H.: Permafrost is warming at a global scale, Nature communications, 10, 264, https://doi.org/10.1038/s41467-018-08240-4, 2019.

Burn, C. R. and Smith, C.: Observations of the "Thermal Offset" in Near-Surface Mean Annual Ground Temperatures at Several Sites near Mayo, Yukon Territory, Canada, ARCTIC, 41, 99–104, https://doi.org/10.14430/arctic1700, 1988.

Dobinski, W.: Permafrost, Earth-Science Reviews, 108, 158–169, https://doi.org/10.1016/j.earscirev.2011.06.007, 2011.

Etzelmüller, B., Guglielmin, M., Hauck, C., Hilbich, C., Hoelzle, M., Isaksen, K., Noetzli, J., Oliva, M., and Ramos, M.: Twenty years of European mountain permafrost dynamics—the PACE legacy, Environ. Res. Lett., 15, 104070, https://doi.org/10.1088/1748-9326/abae9d, 2020.

Fischer, L., Purves, R. S., Huggel, C., Noetzli, J., and Haeberli, W.: On the influence of topographic, geological and cryospheric factors on rock avalanches and rockfalls in high-mountain areas, Nat. Hazards Earth Syst. Sci., 12, 241–254, https://doi.org/10.5194/nhess-12-241-2012, 2012.

Fischer, L., Kääb, A., Huggel, C., and Noetzli, J.: Geology, glacier retreat and permafrost degradation as controlling factors of slope instabilities in a high-mountain rock wall: The Monte Rosa east face, Nat. Hazards Earth Syst. Sci., 6, 761–772, https://doi.org/10.5194/nhess-6-761-2006, 2006.

Garratt, J.: Review: the atmospheric boundary layer, Earth-Science Reviews, 37, 89–134, https://doi.org/10.1016/0012-8252(94)90026-4, 1994.

GCOS: The Status of the Global Climate Observing System 2021: The GCOS Status Report (GCOS-240), World Meteorological Organization, Geneva, Italy, 2021.

Gruber, S. and Haeberli, W.: Permafrost in steep bedrock slopes and its temperature-related destabilization following climate change, J. Geophys. Res., 112, https://doi.org/10.1029/2006JF000547, 2007.

Gruber, S., Hoelzle, M., and Haeberli, W.: Permafrost thaw and destabilization of Alpine rock walls in the hot summer of 2003, Geophys. Res. Lett., 31, n/a-n/a, https://doi.org/10.1029/2004GL020051, 2004.

Gubler, S., Fiddes, J., Keller, M., and Gruber, S.: Scale-dependent measurement and analysis of ground surface temperature variability in alpine terrain, The Cryosphere, 5, 431–443, https://doi.org/10.5194/tc-5-431-2011, 2011.

Gude, M. and Barsch, D.: Assessment of geomorphic hazards in connection with permafrost occurrence in the Zugspitze area (Bavarian Alps, Germany), Geomorphology, 66, 85–93, https://doi.org/10.1016/j.geomorph.2004.03.013, 2005.

Haeberli, W., Noetzli, J., Arenson, L., Delaloye, R., Gärtner-Roer, I., Gruber, S., Isaksen, K., Kneisel, C., Krautblatter, M., and Phillips, M.: Mountain permafrost: development and challenges of a young research field, J. Glaciol., 56, 1043–1058, https://doi.org/10.3189/002214311796406121, 2010.

Harris, C.: Warming permafrost in European mountains, Global and Planetary Change, 39, 215–225, https://doi.org/10.1016/j.gloplacha.2003.04.001, 2003.

Harris, C., Arenson, L. U., Christiansen, H. H., Etzelmüller, B., Frauenfelder, R., Gruber, S., Haeberli, W., Hauck, C., Hölzle, M., Humlum, O., Isaksen, K., Kääb, A., Kern-Lütschg, M. A., Lehning, M., Matsuoka, N., Murton, J. B., Nötzli, J., Phillips, M., Ross, N., Seppälä, M., Springman, S. M., and Vonder Mühll, D.: Permafrost and climate in Europe: Monitoring and modelling thermal, geomorphological and geotechnical responses, Earth-Science Reviews, 92, 117–171, https://doi.org/10.1016/j.earscirev.2008.12.002, 2009.

Harris, S. A., French, H. M., Heginbottom, J. A., Johnston, G. H., Ladanyi, B., Sego, D. C., and van Everdingen, R. O.: Glossary of permafrost and related ground-ice terms, National Research Council of Canada. Associate Committee on Geotechnical Research. Permafrost Subcommittee, ISBN0-660-12540-4, https://doi.org/10.4224/20386561, 1988.

Hartmeyer, Keuschnig M, and Schrott L: Long-term monitoring of permafrost-affected rock faces – A scale-oriented approach for the investigation of ground thermal conditions in alpine terrain, Kitzsteinhorn, Austria, Austrian Journal of Earth Sciences, 105, 128–139, 2012.

Hartmeyer, I., Keuschnig, M., Delleske, R., Krautblatter, M., Lang, A., Schrott, L., Prasicek, G., and Otto, J.-C.: A 6-year lidar survey reveals enhanced rockwall retreat and modified rockfall magnitudes/frequencies in deglaciating cirques, Earth Surf. Dynam., 8, 753–768, https://doi.org/10.5194/esurf-8-753-2020, 2020a.

Hartmeyer, I., Delleske, R., Keuschnig, M., Krautblatter, M., Lang, A., Schrott, L., and Otto, J.-C.: Current glacier recession causes significant rockfall increase: the immediate paraglacial response of deglaciating cirque walls, Earth Surf. Dynam., 8, 729–751, https://doi.org/10.5194/esurf-8-729-2020, 2020b.

Hasler, A., Gruber, S., and Haeberli, W.: Temperature variability and offset in steep alpine rock and ice faces, The Cryosphere, 5, 977–988, https://doi.org/10.5194/tc-5-977-2011, 2011.

Hinzman, L. D., Kane, D. L., Gieck, R. E., and Everett, K. R.: Hydrologic and thermal properties of the active layer in the Alaskan Arctic, Cold Regions Science and Technology, 19, 95–110, https://doi.org/10.1016/0165-232X(91)90001-W, 1991.

Hjort, J., Streletskiy, D., Doré, G., Wu, Q., Bjella, K., and Luoto, M.: Impacts of permafrost degradation on infrastructure, Nat Rev Earth Environ, 3, 24–38, https://doi.org/10.1038/s43017-021-00247-8, 2022.

Hubbart, J., Link, T., Campbell, C., and Cobos, D.: Evaluation of a low-cost temperature measurement system for environmental applications, Hydrol. Process., 19, 1517–1523, https://doi.org/10.1002/hyp.5861, 2005.

IPCC: Summary for Policymakers, in: Masson-Delmotte, V., P. Zhai, A. Pirani, S.L. Connors, C. Péan, S. Berger, N. Caud, Y. Chen, L. Goldfarb, M.I. Gomis, M. Huang, K. Leitzell, E. Lonnoy, J.B.R. Matthews, T.K. Maycock, T. Waterfield, O. Yelekçi, R. Yu, and B. Zhou (eds.).: Climate Change 2021: The Physical Science Basis, Contribution of Working Group I to the Sixth Assessment Report of the Intergovernmental Panel on Climate Change, Cambridge University Press, Cambridge, United Kingdom and New York, NY, USA, 3–32, https://doi.org/10.1017/9781009157896.001, 2023.

James, D. W.: The thermal diffusivity of ice and water between -40 and +60 °C, J Mater Sci, 3, 540–543, https://doi.org/10.1007/BF00549738, 1968.

Kaverin, D., Malkova, G., Zamolodchikov, D., Shiklomanov, N., Pastukhov, A., Novakovskiy, A., Sadurtdinov, M., Skvortsov, A., Tsarev, A., Pochikalov, A., Malitsky, S., and Kraev, G.: Long-term active layer monitoring at CALM sites in the Russian European North, Polar Geography, 44, 203–216, https://doi.org/10.1080/1088937X.2021.1981476, 2021.

Kenner, R. and Phillips, M.: Fels- und Bergstürze in Permafrost Gebieten: Einflussfaktoren, Auslösemechanismen und Schlussfolgerungen für die Praxis: Schlussbericht Arge Alp Projekt ‚Einfluss von Permafrost auf Berg- und Felsstürze‘, WSL-Institute For Snow And Avalanche Research SLF, Graubünden, 2017.

Kim, D. and Oh, S.: Relationship between the thermal properties and degree of saturation of cementitious grouts used in vertical borehole heat exchangers, Energy and Buildings, 201, 1–9, https://doi.org/10.1016/j.enbuild.2019.07.017, 2019.

Krainer, K.: Nationalpark Hohe Tauern: Geologie, 2., überarb. und erw. Aufl., Wissenschaftliche Schriften / Nationalpark Hohe Tauern, Universitätsverlag Carinthia, Klagenfurt, 199 pp., ISBN3853785859, 2005.

Krautblatter, M., Funk, D., and Günzel, F. K.: Why permafrost rocks become unstable: a rock-ice-mechanical model in time and space, Earth Surf. Process. Landforms, 38, 876–887, https://doi.org/10.1002/esp.3374, 2013.

Legay, A., Magnin, F., and Ravanel, L.: Rock temperature prior to failure: Analysis of 209 rockfall events in the Mont Blanc massif (Western European Alps), Permafrost and Periglacial Processes, 32, 520–536, https://doi.org/10.1002/ppp.2110, 2021.

Michaelides, R. J., Schaefer, K., Zebker, H. A., Parsekian, A., Liu, L., Chen, J., Natali, S., Ludwig, S., and Schaefer, S. R.: Inference of the impact of wildfire on permafrost and active layer thickness in a discontinuous permafrost region using the remotely sensed active layer thickness (ReSALT) algorithm, Environ. Res. Lett., 14, 35007, https://doi.org/10.1088/1748-9326/aaf932, 2019.

Miner, K. R., Turetsky, M. R., Malina, E., Bartsch, A., Tamminen, J., McGuire, A. D., Fix, A., Sweeney, C., Elder, C. D., and Miller, C. E.: Permafrost carbon emissions in a changing Arctic, Nat Rev Earth Environ, 3, 55–67, https://doi.org/10.1038/s43017-021-00230-3, 2022.

Nash, J. E. and Sutcliffe, J. V.: River flow forecasting through conceptual models part I — A discussion of principles, Journal of Hydrology, 10, 282–290, https://doi.org/10.1016/0022-1694(70)90255-6, 1970.

Offer, M., Weber, S., Krautblatter, M., Hartmeyer, I., and Keuschnig, M.: Pressurised water flow in fractured permafrost rocks revealed by joint electrical resistivity monitoring and borehole temperature analysis (preprint), https://doi.org/10.5194/egusphere-2024-893, 2024, accepted.

Oke, T. R.: Boundary layer climates, Second edition, Routledge, London, New York, 435 pp., ISBN9780203407219, https://doi.org/10.4324/9780203407219, 1987.

Otto, J., Keuschnig, M., Götz, J., Marbach, M., and Schrott, L.: Detection of mountain permafrost by combining high resolution surface and subsurface information – an example from the glatzbach catchment, austrian alps, Geografiska Annaler: Series A, Physical Geography, 94, 43–57, https://doi.org/10.1111/j.1468-0459.2012.00455.x, 2012.

Outcalt, S. I., Nelson, F. E., and Hinkel, K. M.: The zero-curtain effect: Heat and mass transfer across an isothermal region in freezing soil, Water Resour. Res., 26, 1509–1516, https://doi.org/10.1029/WR026i007p01509, 1990.

PERMOS: Swiss Permafrost Bulletin 2022, Swiss Permafrost Monitoring Network, Noetzli, J. and Pellet, C. (eds.), No. 4, 22 pp., https://doi.org/10.13093/PERMOS-BULL-2023, 2023.

Ravanel, L., Magnin, F., and Deline, P.: Impacts of the 2003 and 2015 summer heatwaves on permafrost-affected rock-walls in the Mont Blanc massif, The Science of the total environment, 609, 132–143, https://doi.org/10.1016/j.scitotenv.2017.07.055, 2017.

Romanovsky, V. E. and Osterkamp, T. E.: Interannual variations of the thermal regime of the active layer and near-surface permafrost in northern Alaska, Permafrost and Periglacial Processes, 6, 313–335, https://doi.org/10.1002/ppp.3430060404, 1995.

Sass, O.: Rock moisture measurements: techniques, results, and implications for weathering, Earth Surf. Process. Landforms, 30, 359–374, https://doi.org/10.1002/esp.1214, 2005.

Schrott, L. ~~Jan-Christoph~~ Otto, J.-C., and ~~Felix~~ Keller, F.: Modelling alpine permafrost distribution in the Hohe Tauern region, Austria, Austrian Journal of Earth Sciences, 169–183, 2012.

Schrott, L., Otto, J.-C., and Keller, F.: Modelling alpine permafrost distribution in the Hohe Tauern region, Austria, Austrian Journal of Earth Sciences, 169–183, 2012.

Smith, M. W. and Riseborough, D. W.: Climate and the limits of permafrost: a zonal analysis, Permafrost and Periglacial Processes, 13, 1–15, https://doi.org/10.1002/ppp.410, 2002.

Stoffel, M., Mendlik, T., Schneuwly-Bollschweiler, M., and Gobiet, A.: Possible impacts of climate change on debris-flow activity in the Swiss Alps, Climatic Change, 122, 141–155, https://doi.org/10.1007/s10584-013-0993-z, 2014.

Streletskiy, D. A., Shiklomanov, N. I., Nelson, F. E., Klene, A. E., Nyland, K. E., and Moore, N. J.: Global Observation Data Show Variable but Increasing Active-Layer Thickness, American Geophysical Union, Fall Meeting, abstract #C016-07, 2020.

Talebi, H. R., Kayan, B. A., Asadi, I., and Hassan, Zahiruddin Fitri Bin Abu: Investigation of Thermal Properties of Normal Weight Concrete for Different Strength Classes, J. Environ. Treat. Tech., ISSN: 2309-1185, 908–914, 2020.

Walter, F., Amann, F., Kos, A., Kenner, R., Phillips, M., Preux, A. de, Huss, M., Tognacca, C., Clinton, J., Diehl, T., and Bonanomi, Y.: Direct observations of a three million cubic meter rock-slope collapse with almost immediate initiation of ensuing debris flows, Geomorphology, 351, 106933, https://doi.org/10.1016/j.geomorph.2019.106933, 2020.

Williams ,P.J. and Smith, M.W.: The frozen earth. Fundamentals of geocryology., Permafrost and Periglacial Processes, 4, 178–181, https://doi.org/10.1002/ppp.3430040221, 1993.